Energy Conversion and Management: X 20 (2023) 100422

Contents lists available at ScienceDirect

Energy Conversion and Management: X

journal homepage: www.sciencedirect.com/journal/energy-conversion-and-management-x

Direct numerical simulation of packed and monolith syngas catalytic combustors for micro electrical mechanical systems

Bahamin Bazooyar [a,b,c,*], Mingming Zhu [c], Vasilije Manovic [c], Seyed Ali Nabavi [c]

[a] Centre for Advanced Powertrain and Fuels, Brunel University London, Uxbridge UB8 3PH, United Kingdom
[b] Department of Mechanical, Aerospace and Civil Engineering (MACE), The University of Manchester, Manchester M13 9PL, United Kingdom
[c] Centre for Renewable and Low Carbon Energy, Cranfield University, Bedford, Bedfordshire MK43 0AL, United Kingdom

ARTICLE INFO

Keywords:
Hydrogen
Catalytic combustor
Combustion
DNS
Flameless
MEMS

ABSTRACT

In this work, a catalytic combustor for micro electrical mechanical system for syngas was designed and analysed using Direct Numerical Simulation (DNS) in conjunction with finite rate chemistry. The effect of catalyst (platinum (Pt), palladium (Pd), palladium oxide (PdO), and rhodium (Rh)), bed type (packed with twelve catalyst shapes and four catalyst monolith), shapes (packed: cylinder, hollow cylinder, four cylinder, single cylinder, single cylinder, cross-webb, grooved, pall-ring, hexagonal, berl-saddle, cube, intalox-saddle, and sphere, monolith: triangular, rectangular, hexagonal, and circular), and operating conditions (inlet temperature and velocity, fuel/air ratio, different concentrations CH_4-H_2-CO) on combustion efficiency and pressure drop were studied using different parameters (combustion efficiency (η), pressure drop, effectiveness factor (Ψ), and fuel conversions (H_2 and CH_4 conversions)). Analysis under different operating conditions reveals that the designed combustor can operate effectively with syngas of varying compositions with a high combustion efficiency of over 85%. Combustion mainly takes place on the surface of the catalyst without gas phase reaction with pressure drops between 18 Pa and 155 Pa. The intalox saddle shape catalysts resulted in the bed effectiveness factor 0.93.[1] The Damköhler for hydroxyl radicals (OH) over the entire length of the reactor is uniformly distributed and well below 3, suggesting uniform combustion.

Introduction

The worldwide demand for generating clean energy necessitates the application of renewable fuels and novel combustion systems [1]. This has spawned a tremendous research effort for microburners as they are compact and efficient for occurrence of combustion under the desired conditions [2]. An effective design of microburners is needed to ensure the autothermal operation of these systems with clean alternative fuels. The catalytic combustors emerge as one of the promising technologies for the occurrence of the combustions in microchannels [3]. They do provide a higher surface area per reactor volume for the chemical reactions, thereby broadening the stability limits [4], facilitating the ignition at low temperatures [5], and suppressing the flame instabilities [6]. Indeed, catalytic combustors enable clean combustion of both low and high calorific values on the surface of the catalyst. The small size of these systems improves the conjugate heat transfer from the reactor body to the preheat zone, stablising the flame [7]. The combustion in catalyst combustors is shared between the gas phase reactions and those under the control on the surface of catalyst. This technology can alter the combustion chemistry by selective adsorption of materials, oxidising the radical on solid surfaces, and desorbing the formed stable gases, thereby limiting the homogeneous reactions [8]. The microburner can also be utilised in chemical reactors, hydrogen generators [9], thermoelectric [10] and thermophotovoltaic [11]. They could provide a reliable source of heat for endothermic processes such as steam reforming and ammonia decomposition when integrated with other microchannel systems to produce fuel cell applications [12].

Conventionally, the occurrence of homogeneous combustion at large scale was used to generate energy [13]. The homogeneous reactions of renewable fuels at the industrial scale are usually challenging as the clean alternative fuel characteristics are usually different from the conventional ones with some like biogas having lower calorific values [14] and the others like hydrogen having wide flammability range and high reactive propensity [15]. These different extreme characteristics of the alternative fuels are limiting factors in the occurrence of

* Corresponding author at: Centre for Advanced Powertrain and Fuels, Brunel University London, Uxbridge UB8 3PH, United Kingdom.
E-mail address: B.bazooyar@brunel.ac.uk (B. Bazooyar).

[1] An ideal reactor effectiveness factor is 1 which 0.5 is equivalent to 100% combustion efficiency and 0.5 is from 0% pressure drop at the combustor outlet.

https://doi.org/10.1016/j.ecmx.2023.100422
Received 27 May 2023; Received in revised form 29 June 2023; Accepted 8 July 2023
Available online 13 July 2023

Nomenclature

Symbols

A	surface area [m^2]
Da	Damköhler number
D	Diameter [m]
E	Equivalent emission
E_f	Fluid energy [J. kg^{-1}]
H	Enthalpy [J. mol^{-1}]
h_o	Heat transfer coefficient [W/m^2 K]
I	Unit matrix
J	Molecular diffusion flux
$\overrightarrow{J}$	Diffusion flux vector
K	thermal conductivity [W/m K]
k_n	Knudsen number
L	length [m]
l^*	characteristic length [m]
P	pressure [pa]
Q	Thermal flux [W/m^2]
R	Production rate of chemical reactions [mol. m^{-3}. s^{-1}]
R	Coefficient of determination
S	catalytic molar production [mol. m^{-2}. s^{-1}]
S	source term [mol. s^{-1}]
Re	Reynolds number
Sc	Schmidt number
T	Temperature [K]
$\overrightarrow{u}$	Velocity vector [$m.s^{-1}$]
X	Mole fraction
Y	Mass fraction

Greek letters

α	Inertial resistance
ρ	Density [kg. m^{-3}]
λ	Mean free path [m]
η	Combustion efficiency
M	Fluid viscosity [kg. $m^{-1}.s^{-1}$]
θ	coverage
σ	Site occupancy
ν	Kinematic viscosity [$m^2.s^{-1}$]
ω	Bed effectiveness components
Ψ	Bed effectiveness factor
Γ	Diffusivity coefficient [$m^2.s^{-1}$]

Subscripts

I	inlet
i, j, k	Species indices
eff	effective
ave	average
w	wall
w, i	wall inlet
w, o	wall outlet

Superscript

h	enthalpy [J]
T	transpose

Abbreviation

CVODE	C-language Variable-coefficients
DEM	Discrete element method
DNS	Direct numerical simulation
EDC	Eddy Dissipation Concept
ER	Equivalence Ratio
FSI	Fluid Solid Interactions
HDPE	High density of polyethylene
LDPE	Low density polyethylene
MEMS	Micro-Electro-Mechanic-Systems
NO_X	Nitrogen oxides
ODE	Ordinary differential equation
OH	hydroxyl radicals
Palladium	Pd
Palladium oxide	Pd-O
Platinum	Pt
PET	Polyethylene terephthalate
Rhodium	Rh
PS	Polystyrene
UHC	Unburned hydrocarbons
VOC	Volatile organic compounds

homogeneous combustion in the majority of practical systems (i.e. boiler, gas turbine) [16], making the conventional combustor designs inept for green fuels. The problems associated with clean alternative fuels are severe in the small-scale micro combustors, purposefully designed to save energy and minimise combustion heat loss. If not carefully designed, the small size of the microcombustors hampers the occurrence of ignition by instigating the radical recombination, extinguishes the flame appearance by dissipating the combustion heat [11]. It can also lead to the blow-off if the outlet velocities transcend the fuel burning velocity [17]. They may also lead to pollutant formation if hydrocarbon chain branching reactions occur without external control, as in conventional combustion systems [18]. Overall, combustion is more under control on the solid surface than in a homogeneous mixture where the chain branching reactions spontaneously take place without any hindrance.

Previous experimentation confirmed that the flame propagation at the microscale is feasible [19] by the interplay among the kinetic and transport of species [20]. Different reactors such as: porous, fixed and fluidised beds have been designed to enhance combustion and diminish the technical problems associated with the micro-scale microburners. Swiss roll burners [21] and porous media are widely used for the catalytic combustion of fuels. The application of renewable fuels, due to their different physical characteristic, for maintaining NOx emissions, effective flow distribution, the combustor's ability to light, tolerate sudden changes in power requirement, efficient combustion, and the achievement of the required life is possible at microscale MEMS combustion systems by a design of catalytic microcombustor. In this work, a new catalytic packed bed reactor for combustion of syngas fuel is designed and analysed in terms of combustion performance and effectiveness under various loads and variables. The operation of the designed reactor is also investigated when loaded with different packings and catalyst monoliths.

Today, the application for carbon capture technologies and renewable energy are at the same order of importance for smooth transition from hydrocarbon based resources [22]. Syngas can be synthesized from variety of feedstocks through different processes [23] and can work as a future fuel and an important hydrogen career for transition from non to renewable energy sources. This work will facilitate the application of hydrogen careers and syngas in small combustors by presenting a novel procedure for design of a catalytic combustor. Sometime, fuel purification could be challenging and production of 100% hydrogen from the gasification process won't turn out techno-economically feasible. In these cases, the utilisation and direct combustion of syngas can be a wise choice for the future design and application of renewable fuels.

Catalytic combustor

A purified syngas gas mixture with 92 wt% methane and 8 wt%

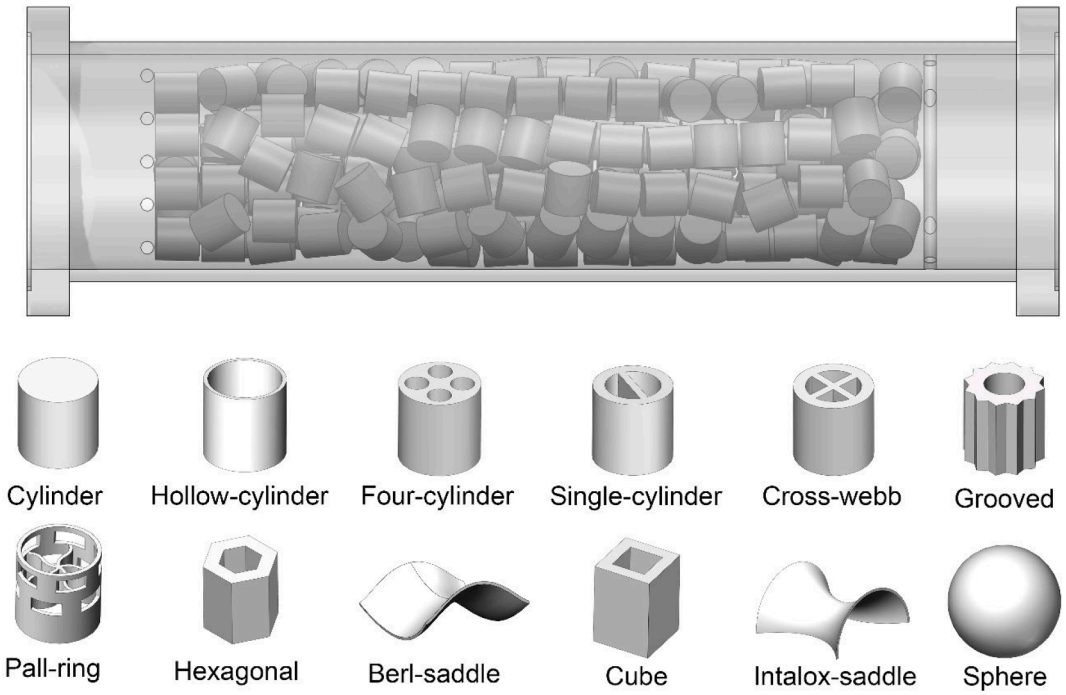

Fig 1. Schematic of the packed bed catalytic combustor and different packing loads for the analysis of the combustion of methane and hydrogen fuel.

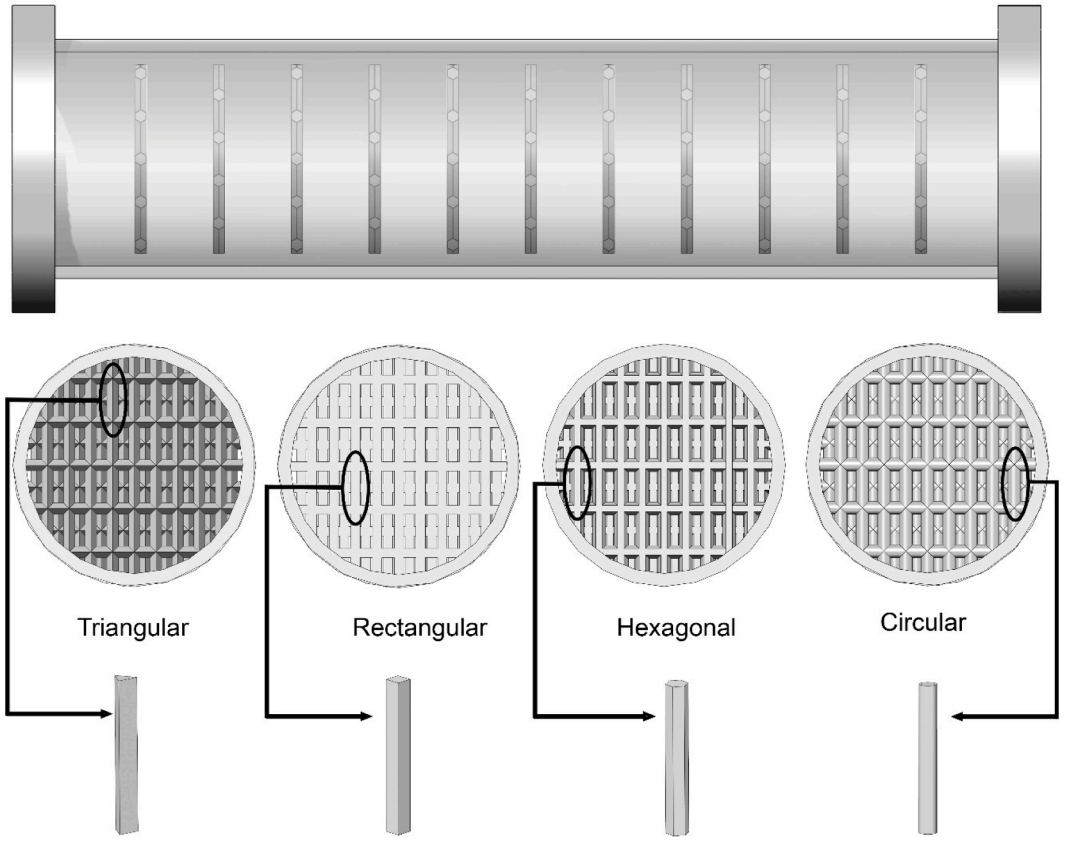

Fig 2. The schematic of catalyst monolith loaded with different catalytic monolith used to load the reactor for catalytic combustion of methane and hydrogen fuel.

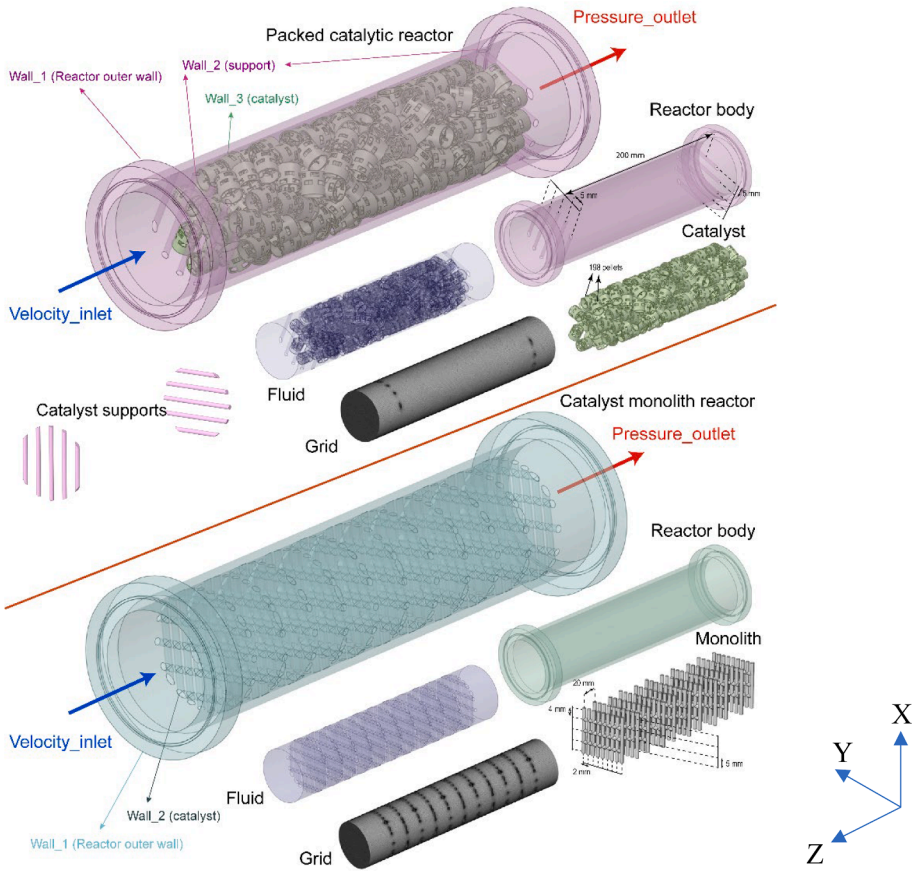

Fig 3. Schematic of the designed packed bed reactor and the circular catalyst monolith, along with their fluid parts extracted, the computational domain made from the reactors fluid, and the boundary conditions in the numerical simulation.

hydrogen was first as a baseline fuel to design the reactor, although syngas with CO and different compositions of species is considered in the sensitivity analysis for show the ability of the combustor to operate with different grades[2] of syngas. This (CH_4: 92 wt% and H_2: 8 wt%) is a baseline which is obtained from the gasification of waste plastic and polymers. The waste material is considered a mixture of polystyrene (PS), high density of polyethylene (HDPE), low density polyethylene (LDPE) and Polyethylene terephthalate (PET) with identical mass composition (each 25%). It is assumed that the CO is fully converted to CH_4 using water–gas shift reaction before considered as a fuel for the catalytic combustor.

The dimensions of the reactor were obtained based on the complete combustion of the fuel/air mixture under equivalence ratio of 0.99 and inlet velocity of 1 ms^{-1} for the premixed mixture syngas/air. This design characteristic will the give the input Re number of 2500. It was envisaged that complete combustion is achieved at the first 1/3 entire length of the combustor with the least pressure drop possible and heat loss. The surface/volume ratios in microburners are usually high [24] making them susceptible to heat loss and low thermal efficiency [25]. The design objective was to control the gas phase reactions so the main contribution in the combustion was from the surface catalyst reactions.

Reactor dimensions

A 220 mm long cylindrical container with an internal diameter of 50 mm was considered for fuel combustion. The thickness of the reactor wall was 3 mm. Two beds support were considered at distances of 20 mm from the reactor inlet and outlet planes. The bed supports are five rows of cylinders, 3 mm in diameter each located at ZX plane near the reactor inlet plane and ZY plane near the reactor outlet plane, respectively. The center-to-center distance of the bed support cylinder was 10 mm. They are well able to limit the movement and transverse of pellets, keeping them at the very middle parts of the combustor. Around 200 pellets (exactly 195) can be placed in the designed reactors. The length and diameter of pellets are both 10 mm. Different shapes for the pellets are assumed to fill the reactor within two bed supports. Fig. 1 gives the schematic of the designed catalytic reactor filled with cylinder types of pellets and other shapes considered for the investigations.

For catalytic monolith reactors, the same cylinder for catalytic beds is exploited to form the body of the combustor. Four different monoliths, namely rectangular, triangular, hexagonal and circular, were employed for the analysis of the combustion, Fig. 2. The circular monolith had a diameter of 3 mm. The other three catalyst monolith has been designed the same way. The triangular, rectangular, and hexagonal catalysts monolith rows were circumscribed within the circle diameter of 3 mm. Two sets of catalysts at two perpendicular planes YZ and XZ, in 11 different columns, placed 18.2 mm from each other, were considered. In the YZ plane, the catalytic part of the reactor is with a column including five rows with a distance of 10 mm. Another column is created at a distance of 18.2 mm from the first one with four rows of catalysts. The latter four rows were placed to cover the space between the two nearby rows of catalysts in the first column. These two sets of columns have been repeated five times along the reactor, with the last column like the first column. For the flow to see the catalyst during the passage of the reactor, more rows of monoliths in every column in XZ plane were added. In the first column, 9 rows of monolith were embedded into the reactor with a center-to-center distance of 5 mm. In the second column,

[2] Grade here connotes different composition of CH_4, H_2 and CO in the syngas.

Table 1
$CH_4/H_2/O_2$/Pt combustion mechanism, $k = AT^n\exp(-E/RT)$.

No	Reaction	A (cm, mol, s)	n	E (kcal mol^{-1})
(R1)	$H_2 + 2PT(S) \Rightarrow 2H(S)$	4.46×10^{10}	0.5	0.0
(R2)	$2H(S) \Rightarrow H_2 + 2PT(S)$	3.70×10^{21}	0.0	67400.0
(R3)	$O_2 + 2PT(S) \Rightarrow 2O(S)$	1.80×10^{21}	−0.5	0.00
(R4)	$O_2 + 2PT(S) \Rightarrow 2O(S)$	2.30×10^{-02}	0.00	0.00
(R5)	$2O(S) \Rightarrow O_2 + 2PT(S)$	3.7×10^{21}	0.00	213200.0
(R6)	$H_2O + PT(S) \Rightarrow H_2O(S)$	7.50×10^{-01}	0.00	0.00
(R7)	$H_2O(S) \Rightarrow H_2O + PT(S)$	1.00×10^{13}	0.00	40300.00
(R8)	$OH + PT(S) \Rightarrow OH(S)$	1.00×10^{00}	0.00	0.00
(R9)	$OH(S) \Rightarrow OH + PT(S)$	1.00×10^{13}	0.00	192800.0
(R10)	$H(S) + O(S) \Leftrightarrow OH(S) + PT(S)$	3.70×10^{21}	0.00	11500.0
(R11)	$H(S) + OH(S) \Leftrightarrow H_2O(S) + PT(S)$	3.70×10^{21}	0.00	17400.0
(R12)	$OH(S) + OH(S) \Leftrightarrow H_2O(S) + O(S)$	3.70×10^{21}	0.00	48200.00
(R13)	$CO + PT(S) \Rightarrow CO(S)$	1.62×10^{20}	*0.5*	*0.00*
(R14)	$CO(S) \Rightarrow CO + PT(S)$	1.00×10^{13}	0.00	125500.0
(R15)	$CO_2(S) \Rightarrow CO_2 + PT(S)$	1.00×10^{13}	0.00	20500.0
(R16)	$CO(S) + O(S) \Rightarrow CO_2(S) + PT(S)$	3.70×10^{21}	0.00	105000.0
(R17)	$CH_4 + 2PT(S) \Rightarrow CH_3(S) + H(S)$	4.63×10^{20}	0.50	0.0
(R18)	$CH_3(S) + PT(S) \Rightarrow CH_2(S)s + H(S)$	3.70×10^{21}	0.00	20000.0
(R19)	$CH_2(S)s + PT(S) \Rightarrow CH(S) + H(S)$	3.70×10^{21}	0.00	20000.0
(R20)	$CH(S) + PT(S) \Rightarrow C(S) + H(S)$	3.70×10^{21}	0.00	20000.0
(R21)	$C(S) + O(S) \Rightarrow CO(S) + PT(S)$	3.70×10^{21}	0.00	62800.0
(R22)	$CO(S) + PT(S) \Rightarrow C(S) + O(S)$	1.00×10^{18}	0.00	184000.0

[a] Averaged for fuel species and hydroxyl at 20Efficiency factor for $\varepsilon_{H_2O} = 12$ and $\varepsilon_{H_2} = 12$.
[b] Troe parameter is $F_c = 0.8$. Efficiency factor for $\varepsilon_{H_2O} = 12$. Efficiency factor for $\varepsilon_{H_2O} = 11$, $\varepsilon_{H_2} = 2$ and $\varepsilon_{O_2} = 0.78$.
[c] (R14) and (R19) are expressed as the sum of the two rate expressions.
[d] Troe parameter is $F_c = 0.5$. Efficiency factor for $\varepsilon_{H_2O} = 12$ and $\varepsilon_{H_2} = 2.5$.

10 rows were considered, so the centre of each monolith in the second column is exactly in the front of the middle point of an imaginary line connecting two centres of the monolith located in the first column. This configuration was to cover all the spaces of the reactor cylinder, so the flow from the inlet sees at least a row of catalyst monolith while passing the reactor. Again, 11 rows of monolith have been created inside the reactor in XZ plane with each 18.2 mm.

Geometry

3-D geometries for both the catalytic bed and catalyst monolith were prepared using SolidWorks 2022 and are demonstrated in Figs. 1 and 2. This forms the solid parts of the computational domain. The volume parts of the model were extracted and forms the computational domain for the combustion modelling and analysis. The solid walls are made of stainless steel 310. The catalyst pellets with coatings: platinum, rhodium, palladium, and palladium and nickel are considered for packing of the microcombustor. Fig. 3 gives the schematic of the solid and fluid parts for pall ring packed bed and circular catalyst monolith. The boundary conditions for solving the governing equations are also presented in Fig. 3. The velocity inlet was used for the inlet boundary condition, and for the outlet, the pressure outlet was used. Three wall types are considered for the packed bed- 1. catalyst wall providing the surface for mass and heat transfer of methane and hydrogen, 2. bed wall for keeping the catalyst in the reactive zone of the microburner, and 3. reactor outer wall for transferring some part of combustion heat to the

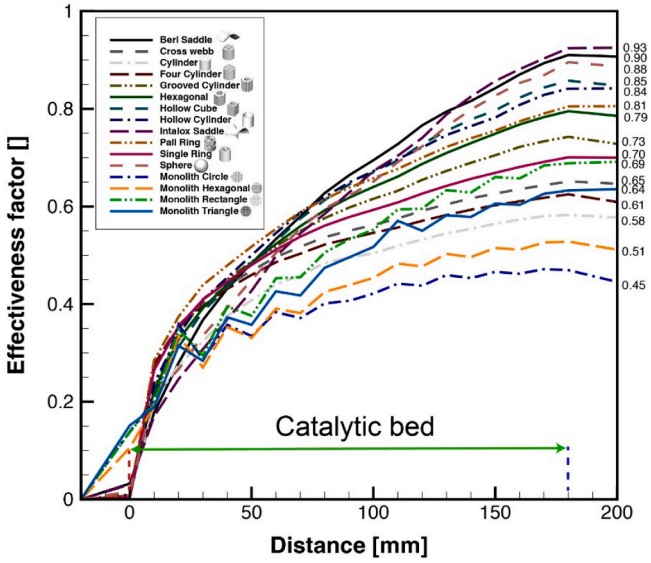

Fig. 5. Effectiveness factor obtained at the designed catalytic reactors 19 transverse plane for different packings and catalytic monolith.

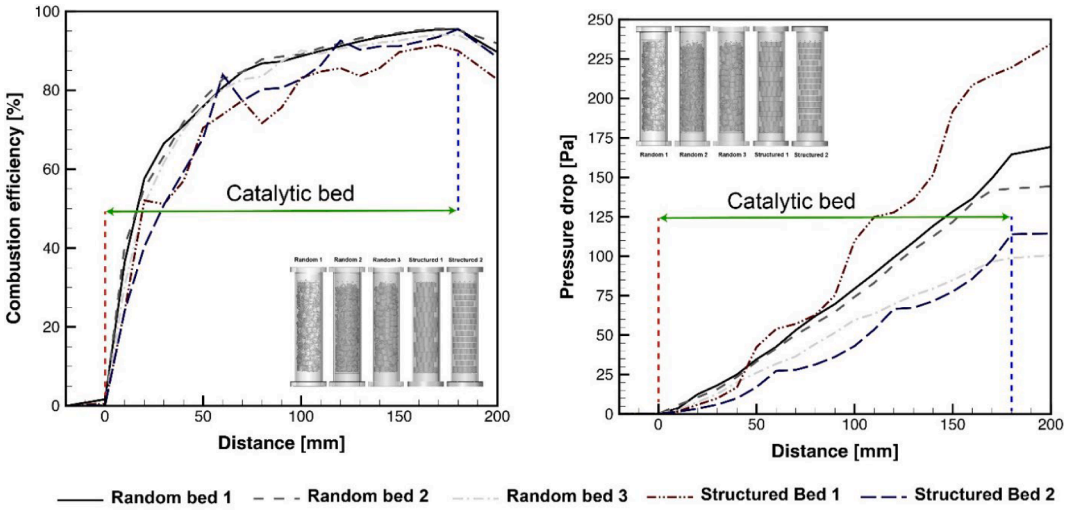

Fig. 4. The combustion efficiency and pressure drop along 19 transverse planes for three random packed beds and two structured beds.

Table 2
Operating conditions for hydrogen combustion in micro combustor.

Shape	Packed bed performance parameter				
	η [\%]]	ΔP [Pa]	Ψ	α	C_2
Berl saddle	87	25.5	0.90	0.33555	0.1255
Cross Webb	93	105.36	0.65	0.00082	3.6375
Cylinder	94	125.33	0.58	0.00020	11.239
Four Cylinder	89	109.55	0.61	0.00096	3.2617
Grooved Cylinder	91	80.13	0.73	0.00122	2.8669
Hexagonal	92	66.33	0.79	0.00151	2.4810
Hollow Cube	91	47.40	0.85	0.00334	1.5119
Hollow Cylinder	96	55.49	0.84	0.01985	0.4861
Intalox Saddle	85.03	18.55	0.93	0.41933	0.1147
Pall ring	92.91	61.91	0.81	0.00169	0.5165
Single ring	94.42	92.69	0.70	0.00118	2.7952
Sphere	89.47	35.07	0.88	0.00090	3.8651
Monolith circle	89.09	154.78	0.45	0.01404	0.6249
Monolith hexagonal	89.66	137.52	0.51	0.02045	0.5285
Monolith rectangle	91.31	90.80	0.69	0.3551	0.3902
Monolith triangle	92	107.05	0.64	0.0851	0.2420

Table 3
Operating conditions for hydrogen combustion in catalytic combustor.

No.	Operation parameter					
	u [m/s]	T [K]	Y_{CH_4}	Y_{H_2}	Y_{O_2}	N
1[a]	1	300	0.05	0.0045	0.23	200
2		350				
3		400				
4		500				
5	0.5					
6	1.5					
7	2					
8			0.0545	0	0.23	
9			0.0327	0.0218	0.23	
10			0.0218	0.0327	0.23	
11			0.0109	0.0436	0.23	
12			0	0.0545	0.23	
13						110
14						50
15						10
16						5

All compositions are mass fractions.
Empty means that the operating point is the same as the base case.
[a] Base case.

environment. In catalyst monolith, just the first and third walls existed in the model, and the support walls are not considered in the simulation. For the catalyst wall, the surface reactions have been defined to represent the absorption, reactions, and desorption of species. Support walls are assumed to be adiabatic. The reactor's outer wall was assumed to have natural convection with air at temperature 283 K and convective heat transfer coefficient (h) 10 W/m^2.K.

Model formulation

The model used for modelling of the combustion is a typical CFD-DEM model. However, the solution of each part (CFD and DEM) was not obtained simultaneously. It was assumed that the packings are stagnant, and the fluid motion does not influence the solids that much, nor the solid particles random movement influence the fluid. The fluid movement was considered turbulent, although the upstream Reynolds number is around 2500 which is at the transition state. The DEM models were used for preCFD modelling and generation of the computational domain. The reactor monolith catalytic structures are considered stagnant as they are fixed over particular shapes entrenched and embedded into the body of the reactor. For this work, the pellets are also located carefully between two sets of supports, one at the beginning of the and the other at the very end of the reactor. The DEM was used to provide the

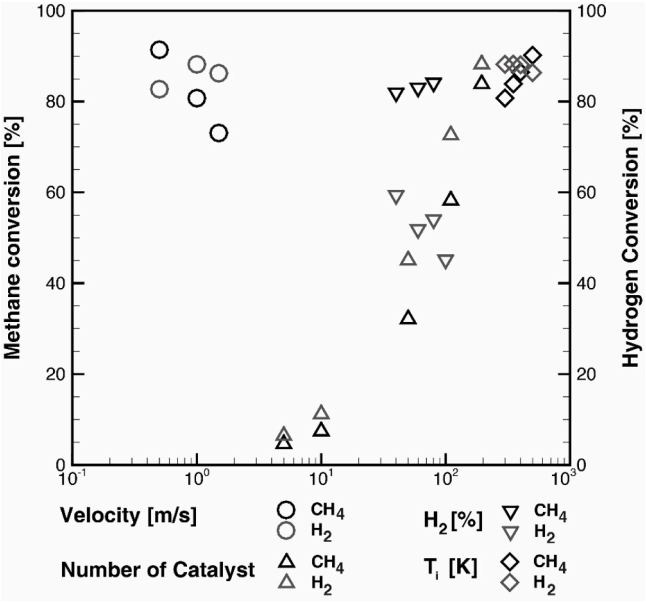

Fig. 6. The operating graph of the catalytic reactor in terms of methane and hydrogen conversion in relation to premixed reactant velocity, temperature, percentage of hydrogen and number of catalysts in the bed.

Table 4
The surface combustion mechanisms on different catalyst pellets.

Fuel	Catalyst	No of reac.	Ref
CH_4/H_2	Platinum [Pt]	22	[26]
H_2	Rhodium [Rh]	12	[42]
H_2	Palladium [Pd]	13	[43]
CO	Rhodium [Rh]	10	[44]
CH_4/H_2	Palladium [Pd]	54	[45]
CH_4/H_2	Palladium oxide [PdO]	77	[46]

randomness in the structure of packings when they were loaded by different spatial orientation via Newton's laws of motion. The combusting gas flow will impact and may cause some vibrational and some slight rotational but not really apparent translational movement. This might lead to a solid-fluid interaction (FSI) that should be considered in the modelling. However, in this work, for a matter of simplicity the FSI are not considered in the modelling as we aim to offer a design that in the packed solids are fixed and stagnant.

Governing equations

The conservation equations for mass, momentum, total internal energy (E), and species mass fractions, Y_j for (N-1) chemical species in a low Mach incompressible format are defined for the gas phase. The equations with standard notations are:

The mass balance:

$$\frac{\partial \rho}{\partial t} + \nabla.(\rho \vec{u}) = 0 \tag{1}$$

The momentum balance:

$$\frac{\partial \rho \vec{u}}{\partial t} + \rho(\vec{u}.\nabla \vec{u}) = -\nabla p + \nabla.\left(\mu\left[\nabla \vec{u} + (\nabla \vec{u})^T - \frac{2}{3}\nabla.\vec{u}I\right]\right) \tag{2}$$

The energy balance:

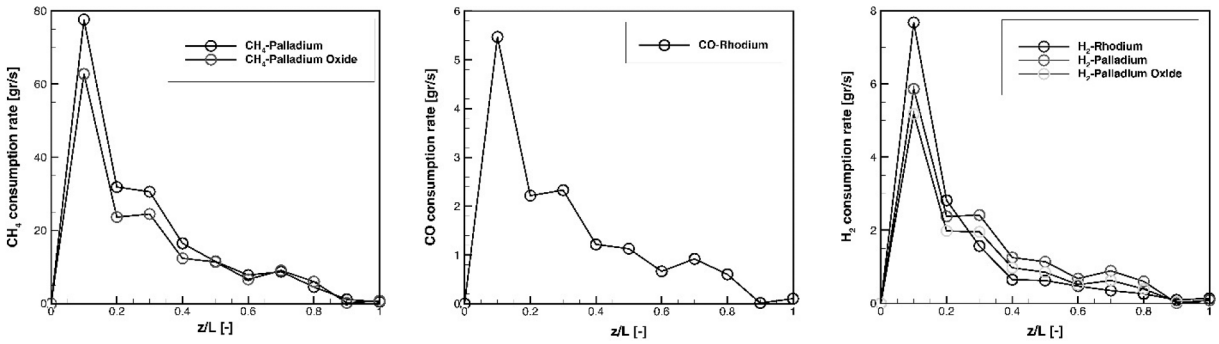

Fig. 7. The time averaged rate of fuel consumption along the reactor dimensionless length for catalytic combustion of h_2-Rhodium, H_2-Palladium, and CO-Rhodium for intalox packing.

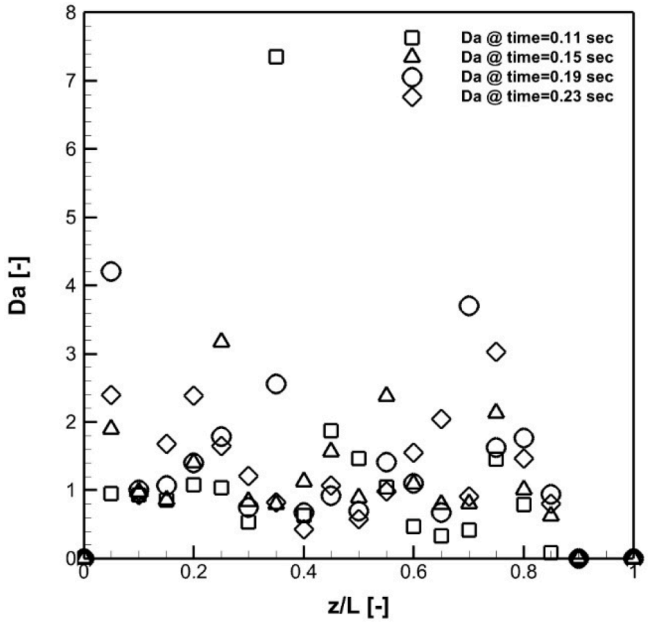

Fig. 8. Temporal evolution of da for ch_4, H_2 and OH at physical times 0.03, 0.04, 0.07, 0.11, 0.15, 0.23 averaged at 20 transverse planes along the reactor length.

$$\frac{\partial \rho E}{\partial t}+\nabla.\vec{u}\left(\rho E_f+p\right)=\nabla.\left[k_{eff}\nabla T-\left(\sum_j h_j\vec{J_j}\right)+\left(\mu\left[\nabla\vec{u}+(\nabla\vec{u})^T-\frac{2}{3}\nabla.\vec{u}I\right].\vec{u}\right)\right]+S_f^h \tag{3}$$

The gaseous species transport:

$$\frac{\partial \rho Y_j}{\partial t}+\nabla.\left(\rho\vec{u}Y_j\right)=-\nabla\vec{J_j}+R_j,\alpha\ =\ 1,\ldots,\mathrm{N}\text{ - }1 \tag{4}$$

The surface species:

$$\frac{\partial \theta_k}{\partial t}=\sigma_k\frac{\dot{s}_k}{\Gamma}\ \mathrm{k}\ =\ 1,\ldots,\mathrm{N}_s \tag{5}$$

These sets of equations are closed using the equation of state (EOS), which in this study is assumed as the ideal gas, considering the temperature is high enough for the gas to have negligible intermolecular forces.

$$p_0=\frac{\rho RT}{\overline{W}}\overline{W}=\frac{1}{\sum_{i=1}^{N_g}\frac{Y_i}{W_i}} \tag{6}$$

To model the catalytic reaction along with the gas phase flow, The diffusion terms in the species equation were modelled using:

$$-\nabla\vec{J_j}=-\nabla\left(\rho Y_j\underline{V_j}\right) \tag{7}$$

In this equation, the diffusion term was modelled based on the gas phase diffusion velocity, $\underline{V_j}$:

$$\underline{V_j}=\widetilde{\underline{V_j}}+\underline{V_c} \tag{8}$$

$\underline{V_c}=\sum_{i=1}^{N}Y_j\widetilde{\underline{V_j}}$ indicates the correction velocity which is added to ensure the conservation of mass. $\widetilde{\underline{V_j}}$ is obtained from the mixture-averaged diffusion model:

$$\widetilde{\underline{V_j}}=-\left(D_j/X_j\right)\underline{\nabla}X_j \tag{9}$$

where D_j indicates *j*th species mixture-averaged diffusivity and X_j denotes the *j*th mole fraction.

The following boundary condition between the gas-phase and gas-wall interface are considered:

$$J_{j,w}=\underline{n}.\rho Y_i\left(\underline{u}+\underline{V_j}\right)\Big|_w=\dot{s}_i w_i,\ \mathrm{j}\ =\ 1,2,\ldots,\mathrm{N} \tag{10}$$

$\dot{s}_i$ represents the molar catalytic production rate, $J_{j,w}$ indicates the mass flux normal to the wall for the jth gas-phase species, $\underline{n}$ denotes the outward normal vector at the catalyst surface, and $\underline{u}\Big|_w$ is the Stefan velocity, given by:

$$\underline{n}.\underline{u}\Big|_w=\frac{1}{\rho}\sum_{i=1}^{N}\dot{s}_i W_i,\ \mathrm{i}\ =\ 1,\ldots,\mathrm{N}_g. \tag{11}$$

Combustion chemistry

For the steady simulation, wall temperature was observed on the catalyst surface around T_w = 1290 K. This temperature is chosen in design optimisation phase testing different surface catalyst temperature to find one with maximum effectiveness factor while it leads to the expected combustion state. This gives the average temperature of the $T_{average\_volumetric}$ = 800 K for the mixture in the reactor which is well below the minimum temperature required for lean combustion of methane and hydrogen. The numerical simulation with and without the gas-phase reactions leads to insignificant difference based on preliminary calculations in the species concentrations in the reactor. Hence, only the surface reactions were considered for design and modelling of the reactor. For this study, the detailed catalytic chemistry reactions by Deutschmannet al. [26] has been used to simulate the catalytic combustion and design of the reactor. The reaction, given in Table 1, includes 8 volumetric, 11 sites and 1 solid species.

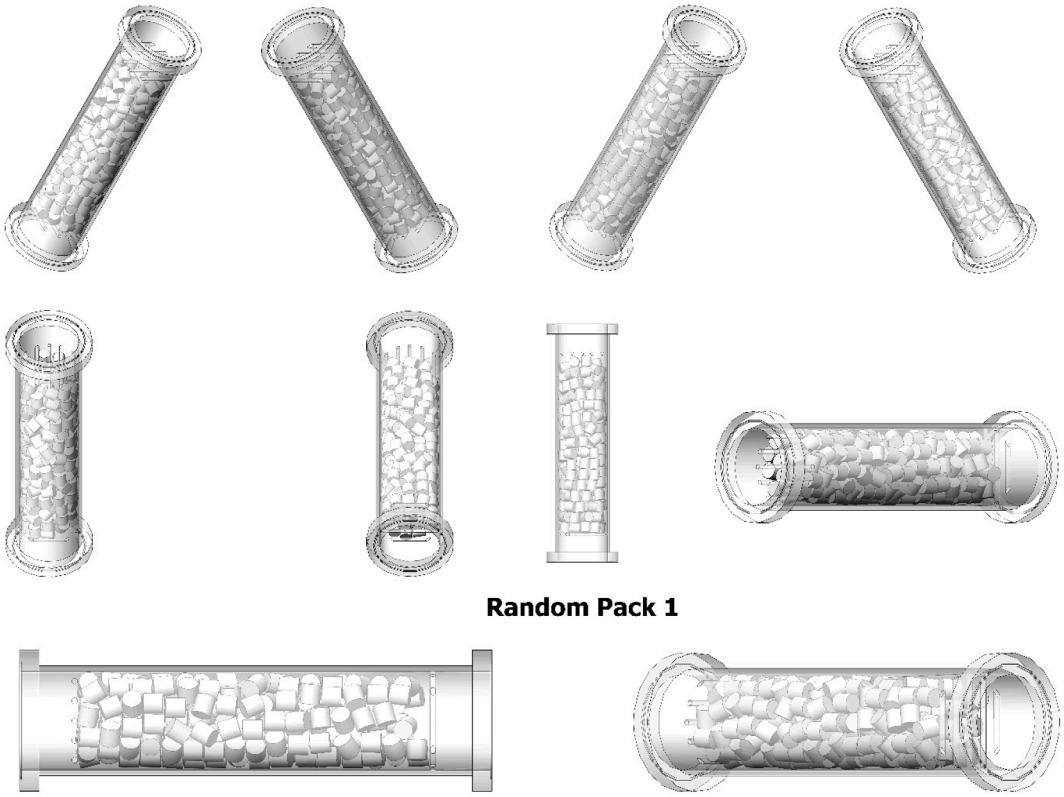

Fig. A1. The designed combustor random pack 1 different views.

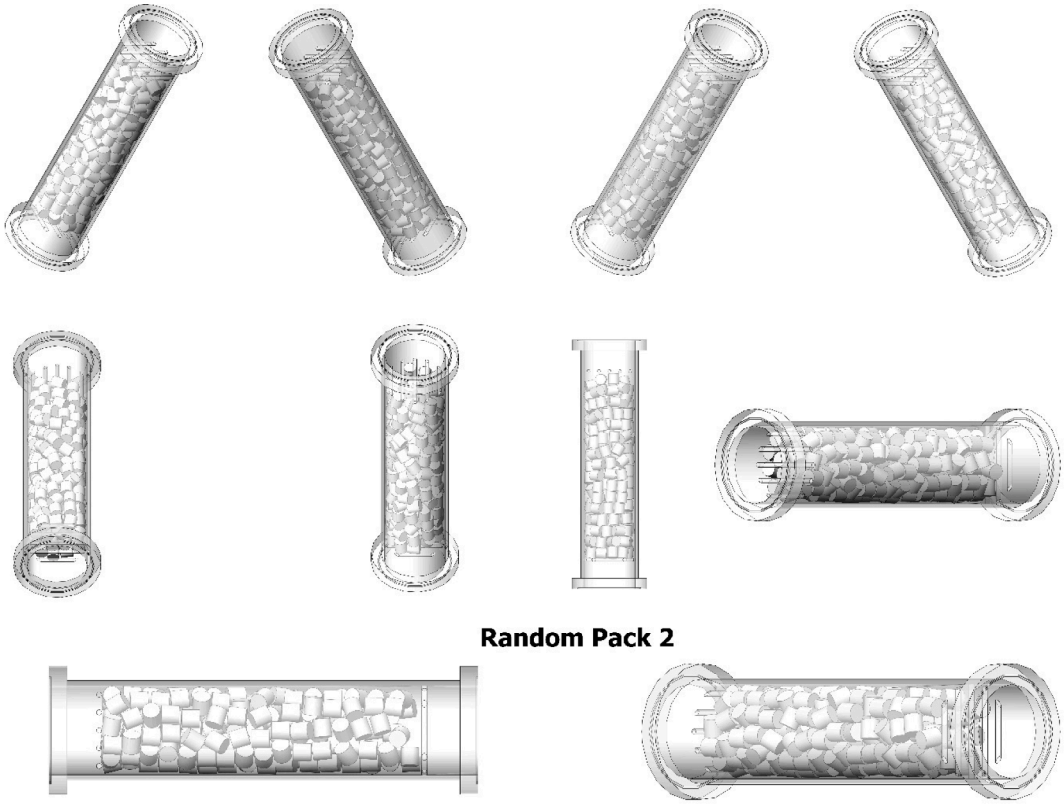

Fig. A2. The designed combustor random pack 2 different views.

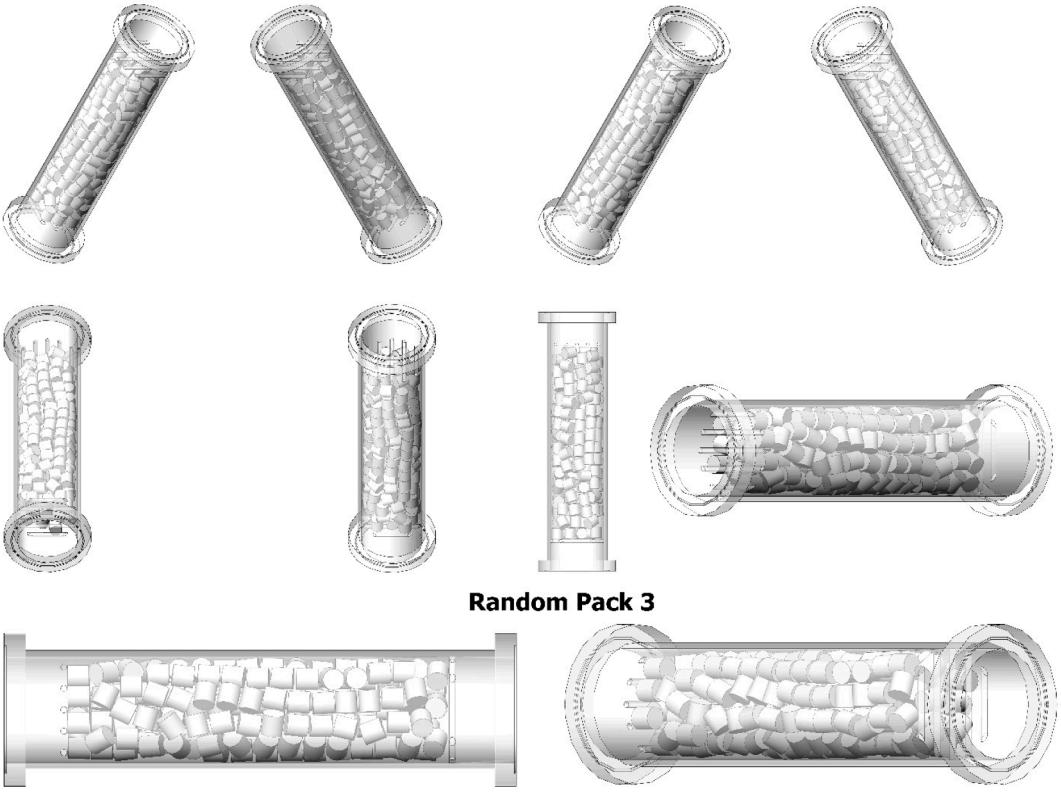

Fig. A3. The designed combustor random pack 3 different views.

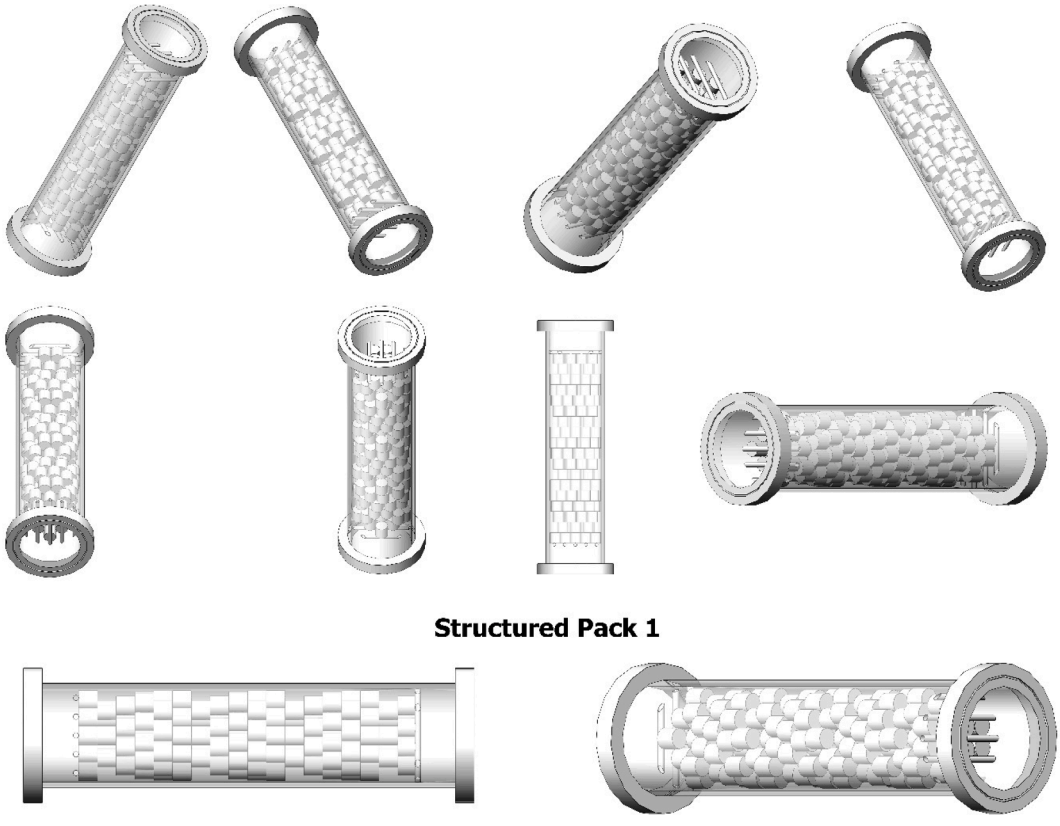

Fig. B1. The designed combustor structured pack 1 different views.

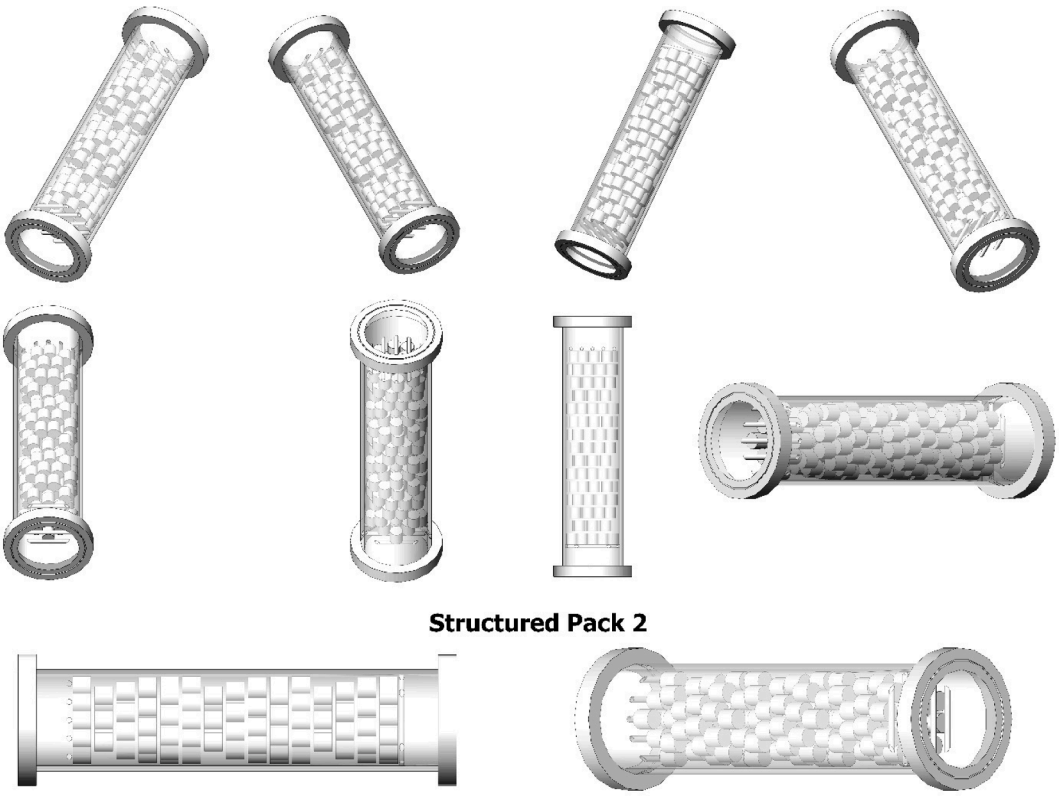

Fig. B2. The designed combustor structured pack 2 different views.

Numerical method

Solution algorithm

The computational domain including the volumetric space for the transverse motion of the syngas reactive mixture is segregated into the hexahedral elements with identical surfaces and dimensions. The conservation equations are separated using a high-order splitting scheme [27] and are discretised using Nth-order Legendre-Lagrangian polynomial [28] to give the solution in each spatial dimensions. The thermochemical state of the microcombustor is resolved using the implicit stiff ODE integrator CVODE [29]. For this work, the reaction source terms in the gas and surface are directly solved although they are massive sets of stiffs ODEs.

The analysis of this work includes the findings of 44 independent different simulations. Five distinct numerical analysis is associated with the different strategies for packing the bed (randomness or structured. Sixteen simulations belong to the structural analysis of the reactor for different catalyst types (monolith and packed beds). Another sixteen sets are for the optimisation of the reactor and analysis at different operating points which gives the operating line of the reactor at different variable loads, different fuel grades, different number of catalytic pellets, and different syngas grades.

Computational domain

Since the flow is considered turbulent, the domain with a high resolution of elements is considered for the simulations. The reactor fluid part, i.e., computational domain, is split into several conforming hexahedral elements. In span-wise direction x-direction, the domain is discretized into semi-uniform 30 elements. Around 35 elements are clustered close to the wall in spanwise-y direction (r-direction) near the combustor walls and catalyst surface. Around 500 uniform elements in the streamwise-z direction z are allocated to the domain. The discretization was done using the seventh order interpolating for each element in spatial directions. This gives a total number of 180,000,000 grid points. The resolution of the domain is most exhaustive in the proximity of catalyst pellets and monolith where adsorption-reactions-desorption are taking place. The parameters, values and variables are normalized and non-dimentionalised using associated boundary and initial conditions before solving the governing equations and presentation of results.

Results and discussion

Effect of catalyst packing

The operation of the designed reactor is evaluated for different ways for loading the bed with catalyst. Three random structures and two structured versions of the microcombustor filled with only cylinder catalyst type have been prepared and analysed in terms of pressure drop and combustion efficiency. The minimum pressure drops, and a maximum combustion efficiency are desired for both stationary and mobile combustion systems. Fig. 4 gives the trend of pressure drop and combustion efficiency along the reactor from inlet to outlet. The dp and CE were averaged at 19 planes perpendicular of the flow direction and inlets and outlet planes. The schematic of the reactors has also been shown in a small subgraph within the trendline box.

The random structures are the same in number 195 and different in the orientation and arrangement of catalysts in the reactor. The two structured packed reactors are different in number of catalysts and spaces between catalysts in each row of the reactors. In structured reactor number 1, the catalysts were placed at the top of those below without any space considering for each row of catalysts. This reactor includes 200 catalysts. In structured reactor number 2, the catalysts were placed in series of sieves each with distance 2 mm from the bottom catalysts, therefore there is a gap between every series of catalysts in the reactor. The number of catalysts in this reactor is 171.

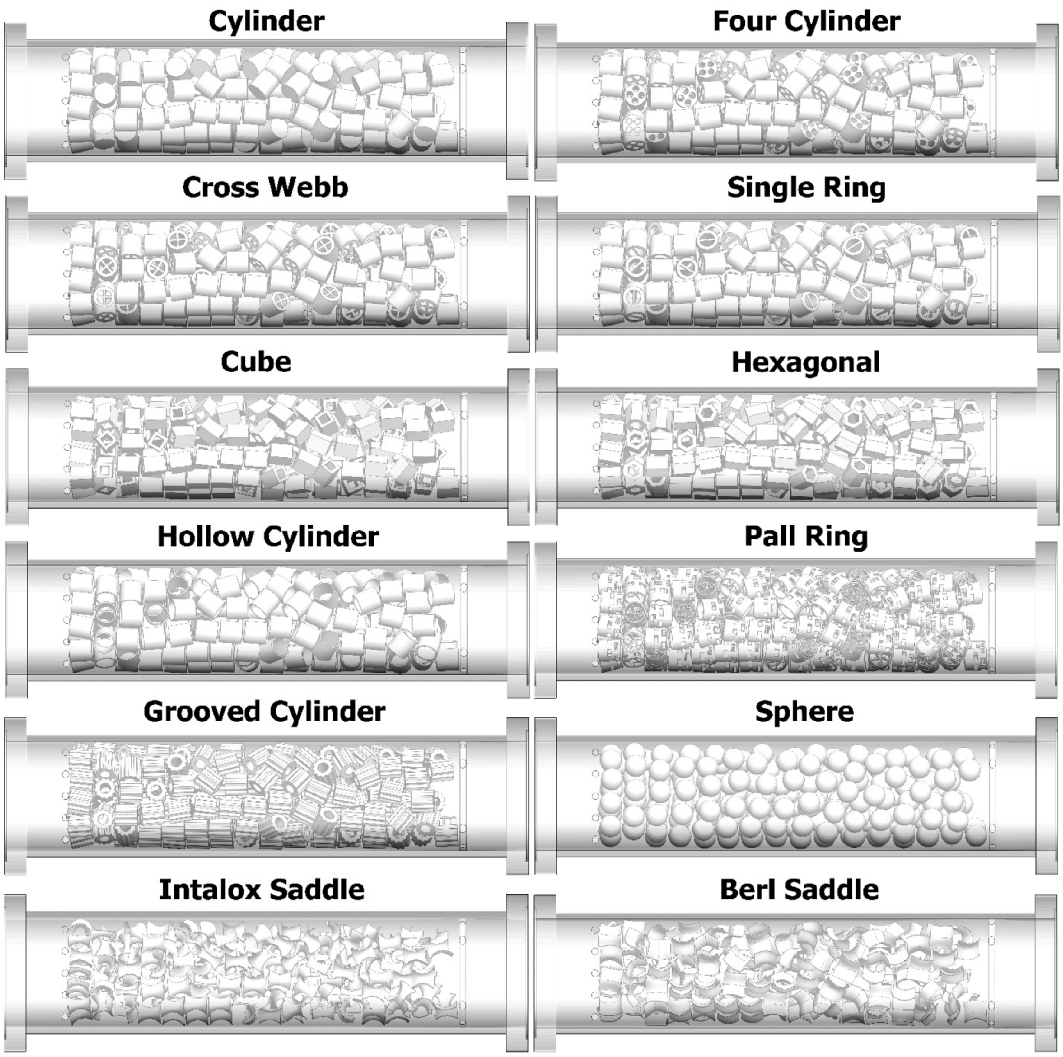

Fig. C1. The designed combustor packing illustration (packed: cylinder, hollow cylinder, four-cylinder, single cylinder, single cylinder, cross-webb, grooved, pall-ring, hexagonal, berl-saddle, cube, intalox-saddle, and sphere).

The results demonstrate that the combustion of $CH_4 + H_2$ completes along the 180 mm length of both the random and structured packed reactor. The combustion efficiency of the random beds 1, 2, and 3 reaches the values 90%, 92%, and 89% at the combustor outlet plane. The combustion efficiency of the structured beds 1 and 2 go up to the value of 83% and 88% at the reactor outlet. The pressure drops, however, for the studied reactors are quite different. In terms of pressure drop, maximum pressure drop is for the structured bed 1 although the catalysts are perfectly arranged within the reactor body. Indeed, the reactor volume is playing the main role in the pressure drop. The reactor with the most space available for the reacting mixture has the least pressure drop and vice versa. The restriction and constriction of flow increases the inter-catalytic fluid velocity, thereby decreasing the pressure of the fluid. The free volume inside the structured packed reactor 1 and 2 is 312 and 335 mm^3, respectively. For random packed reactors, the free volume of the reactor is 316 mm^3.

Note that the combustion efficiency within [83 95]% is comparable to the combustion efficiency of industrial scale gensets [30–33] and other micro combustor units (microturbine combustors: [34]). The net combustion efficiency of diesel fuel and biodiesels is obtained more than 90% [33]. In microgas turbines the combustion efficiency of nearly 100% [35] could be obtained as the air staging leaves no room for poor mixing and insufficient combustion [36]. In conventional combustor, an air swirler is implemented to improve the mixing and reduction of nitrogen oxides [37,38]. Here, the mixing is achieved by bifurcation and microchanneling of the fluid over the catalyst surface. This improves the rate of adsorption and catalytic reactions.

Effects of catalyst shape

For mechanical devices, the pressure drop along with combustion efficiency is important for the efficient operation of MEMS. The effectiveness factor has been defined to give both the contribution of the pressure drop and combustion efficiency. The ideal reactor is with effectiveness factor 1 which both satisfies the 0.5 for combustion efficiency and pressure drop. The definition of the effectiveness factor (Ψ) is given:

$$\Psi = \omega_{Combustionefficiency} + \omega_{Pressuredrop} \tag{12}$$

The contribution of the combustion efficiency ($\omega_{Combustion\ efficiency}$) is universal and represent the heat loss by unburned materials. It is simply half of the combustion efficiency value. The contribution from the pressure drops ($\omega_{\text{Pressure drop}}$) is specific to this study which gives the value 0 for the reactor with maximum pressure drop and the value 1 for reactor with minimum pressure drop. It is also distributed within [0 0.5] similar to $\omega_{Combustion\ efficiency}$ from inlet to outlet. Such a definition gives the effect of packing on both the pressure drop and combustion efficiency.

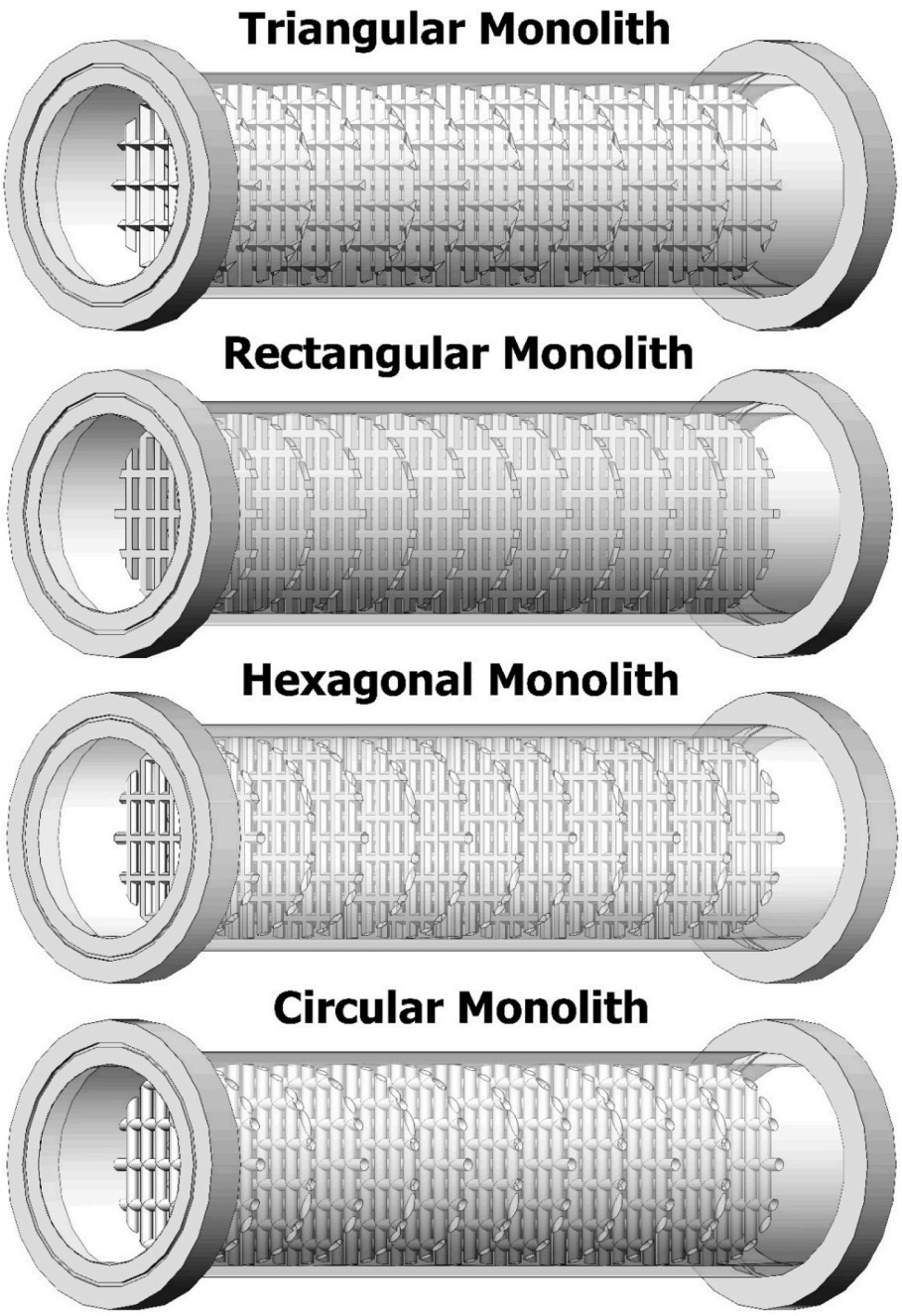

Fig. D1. The designed combustor packing illustration (monolith: triangular, rectangular, hexagonal, and circular).

$$\Psi = \left(\frac{0.169008[OH] + 0.21[H_2O]}{[OH] + [H_2O] + [H_2]} + \frac{0.18705[CO] + 0.29[CO_2]}{[CO_2] + [CO] + [CH_4]}\right) + \frac{\Delta P_{Reactor,local}\left(\Delta P_{maximum} - \Delta P_{Reactor,outlet}\right)}{2\Delta P_{Reactor,outlet}(\Delta P_{maximum} - \Delta P_{Minimum})} \quad (13)$$

where [X] denotes either the mole fraction or mole concentration of the specie X, $\Delta P_{maximum}$ and $\Delta P_{Minimum}$ are constant and represent the maximum and minimum pressure drop for the reactor with all investigated packings. In this study, $\Delta P_{maximum}$ is for the monolith circle with 155 Pa and $\Delta P_{\mathrm{Minimum}}$ belongs to the intalox saddle packing with 18 Pa. $\Delta P_{Reactor,local}$ and $\Delta P_{\mathrm{Reactor,outlet}}$ specify the local, i.e., spatial, pressure drop at pressure drop at the reactor outlet.

The spatial effectiveness factor for the catalytic and monolith reactor is given Fig. 5. The intalox and berl saddles provide the effectiveness factor 0.93 and 0.90, respectively which is higher than other packings. The analysis has shown that the combustion efficiency for all the packings and monolith reaches almost the value 1 at the combustor outlet plane. Thus, the effectiveness factor for this reactor is more under the influence of pressure drop along the catalytic beds. The catalytic monoliths have the minimum effectiveness factor although their combustion efficiency is slightly higher than any other packings.

The inertial resistance ($\alpha = \frac{D_p^2}{150}\frac{\varepsilon^3}{(1-\varepsilon)^2}$) and viscous resistance ($C_2 = \frac{1.75\rho}{D_p}\frac{(1-\varepsilon)}{\varepsilon^3}$) are two parameters that can be used to evaluate the operation of packed beds, catalyst monolith or other porous medium. For this reactor, the effectiveness factor is a direct function of the inertial resistance and inverse function of the viscous resistance. Indeed, the

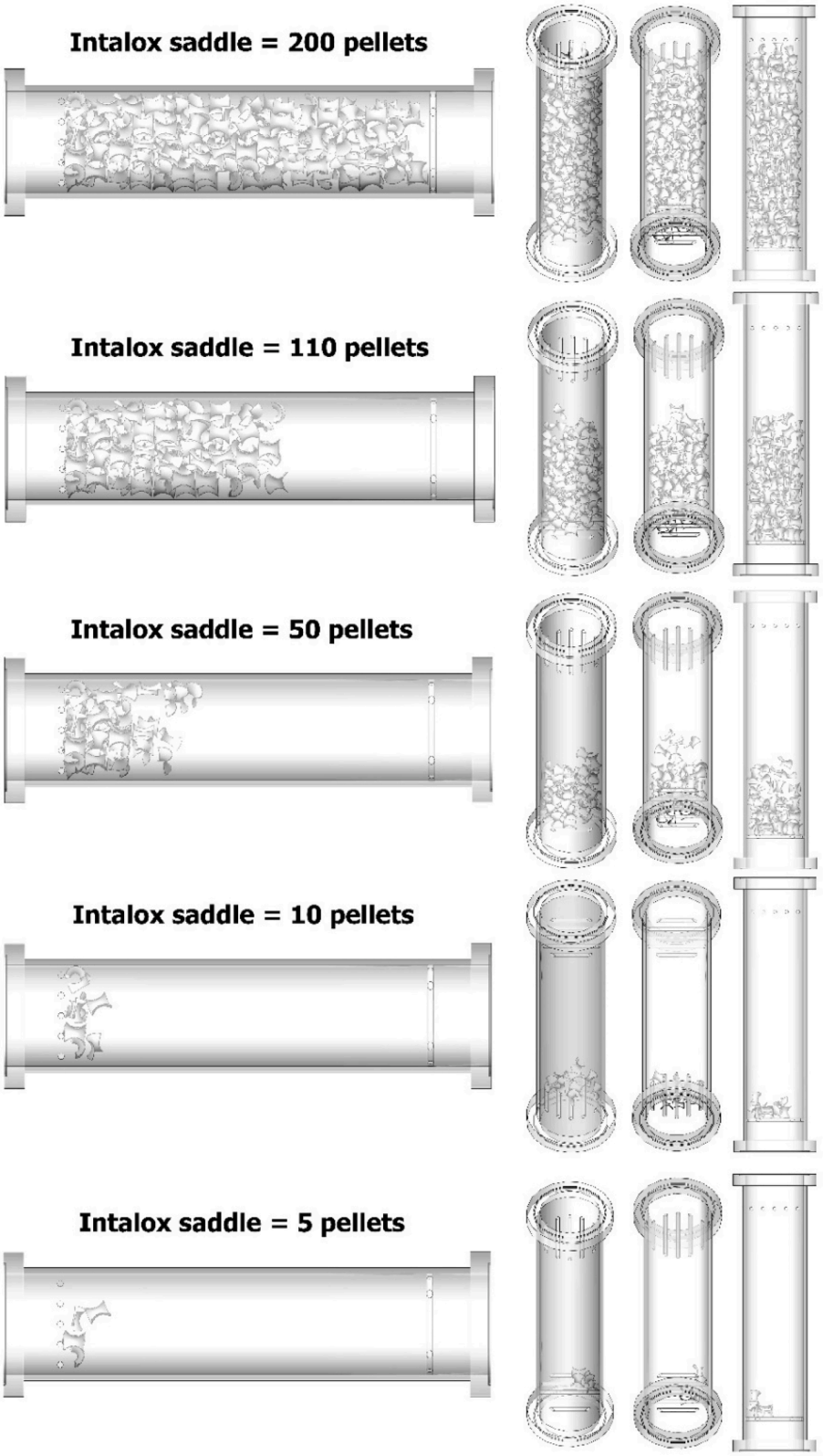

Fig. E1. The designed combustor packed with Intralox Saddle with different numbers of pellets illustration.

presence of more pore volume in the case of saddle packing gives rise to their highest effectiveness factor and their better performance for catalytic combustion. Table 2 gives the combustion efficiency, pressure drop, effectiveness factor, inertial and viscous resistance for different packings loaded into the designed reactor at the outlet plane. The combustion efficiency for hollow cylinder, single ring and cylinder is noticeably higher than any other packings, although they are in the middle hierarchy of packings in terms of effectiveness factor.

Table F1
H_2/O_2/Pd combustion mechanism, $k = AT^n\exp(-E/RT)$.

No	Reaction	A (cm, mol, s)	n	E (kJ mol^{-1})
	$H_2 + 2Pd => 2H(s)$	0.70	0.0	0.0
	$2H(s) => H_2 + 2Pd(s)$	$4.800\times10^{+21}$	0.0	84.0
	COV/H(s)	0.0	0.0	−15.0/
	$H + Pd(s) => H(s)$	1.00	0.0	0.0
	$O_2 + 2Pd(s) => 2O(s)$	0.400×10^{-00}	0.0	0.0
	$2O(s) => O_2 + 2Pd(s)$	$7.100\times10^{+21}$	0.0	230.0
	$O + Pd(s) => O(s)$	1.00	0.0	0.0
	$H_2O + Pd(s) => H_2O(s)$	0.75	0.0	0.0
	$H_2O(s) => H_2O + Pd(s)$	$1.300\times10^{+13}$	0.0	44.0
	$OH + Pd(s) => OH(s)$	1.00	0.0	0.0
	$OH(s) => OH + Pd(s)$	$1.300\times10^{+13}$	0.0	213.0
	$H(s) + O(s) = OH(s) + Pd(s)$	$3.70\times10^{+21}$	0.00	11.5
	$H(s) + OH(s) = H_2O(s) + Pd(s)$	$3.70\times10^{+21}$	0.00	17.4
	$OH(s) + OH(s) = H_2O(s) + O(s)$	$3.70\times10^{+21}$	0.00	48.2

Table F2
H_2/O_2/Rh combustion mechanism, $k = AT^n\exp(-E/RT)$.

No	Reaction	A (cm, mol, s)	N	E (kJ mol^{-1})
(R1)	$H_2 + Rh(s) + Rh(s) => H(s) + H(s)$	3.000×10^{-02}	0.000	0.000
(R2)	$O_2 + Rh(s) + Rh(s) => O(s) + O(s)$	1.000×10^{-02}	0.000	0.000
(R3)	$H_2O + Rh(s) => H_2O(s)$	1.000×10^{-01}	0.000	0.000
(R4)	$H(s) + H(s) => Rh(s) + Rh(s) + H_2$	$5.574\times10^{+19}$	0.239	59.691
(R5)	$O(s) + O(s) => Rh(s) + Rh(s) + O_2$	$5.329\times10^{+22}$	−0.137	386.995
(R6)	$H_2O(s) => Rh(s) + H_2O$	$6.858\times10^{+14}$	−0.280	44.993
(R7)	$O(s) + H(s) => OH(s) + Rh(s)$	$8.826\times10^{+21}$	−0.048	73.365
(R8)	$OH(s) + Rh(s) => O(s) + H(s)$	$1.000\times10^{+21}$	0.045	48.041
(R9)	$OH(s) + H(s) => H_2O(s) + Rh(s)$	$1.743\times10^{+22}$	−0.127	41.731
(R10)	$H_2O(s) + Rh(s) => OH(s) + H(s)$	$5.408\times10^{+22}$	0.129	98.220
(R11)	$OH(s) + OH(s) => O(s) + H_2O(s)$	$5.736\times10^{+20}$	−0.081	121.594
(R12)	$O(s) + H_2O(s) => OH(s) + OH(s)$	$1.570\times10^{+22}$	0.081	203.407

Effect of inlet velocity, H_2 concentration, temperature, and number of pellets

One important criterion which shows the operation of the reactor under possible variable loads, catalyst inactivity, temperature oscillation and fuel type is the operating graph of the catalytic reactor. The operating graph is obtained for this designed reactor from the simulations of Table 3 to show how the conversation of methane and hydrogen is influenced by the inlet jet velocity, inlet temperature, reactor number of pellets and percentage of hydrogen in the fuel stream.

Fig. 6 demonstrates the operating graph in terms of CH_4 and hydrogen conversations in relation to the velocity, temperature, number of catalyst in the bed and H_2 volumetric percentage in the fuel stream. The graph has two markers-1. Black showing the conversion of methane and 2- Gray showing the hydrogen conversion. The logarithmic X-axis could be velocity, number of catalysts in the reactor, inlet temperature, and hydrogen percentage in the reactant.

The operating graph exhibits the conversion trendlines over number of catalysts and hydrogen percentage to be more deterministic of the methane and hydrogen conversion. When the number of catalysts goes below 100, the conversion of methane and hydrogen significantly diminishes. For feed hydrogen percentage, the situation is different. When the volumetric percentage of hydrogen in the fuel is going from 30% to 100%, the H_2 conversion is fixed within [50 60], although the conversion of methane regardless of feed hydrogen percentage is as high as

Table F3
CO/O_2/Rd combustion mechanism, $k = AT^n\exp(-E/RT)$.

No	Reaction	A (cm, mol, s)	n	E (kJ mol^{-1})
(R1)	$O_2 + Rh(s) + Rh(s) => O(s) + O(s)$	1.000×10^{-02}	0.000	0.000
(R2)	$CO_2 + Rh(s) => CO_2(s)$	4.800×10^{-02}	0.000	0.000
(R3)	$CO + Rh(s) => CO(s)$	4.971×10^{-01}	0.000	0.000
(R4)	$O(s) + O(s) => Rh(s) + Rh(s) + O_2$	$5.329\times10^{+22}$	−0.137	386.995
(R5)	$CO(s) => Rh(s) + CO$	$1.300\times10^{+13}$	0.295	134.070
	COV/CO(s)	$0.000\times10^{+00}$	0.000	−47.000/
(R6)	$CO_2(s) => Rh(s) + CO_2$	$3.920\times10^{+11}$	0.315	20.505
(R7)	$O(s) + C(s) => CO(s) + Rh(s)$	$1.173\times10^{+22}$	0.000	92.142
(R8)	$CO(s) + Rh(s) => O(s) + C(s)$	$6.390\times10^{+21}$	0.000	174.758
	COV/CO(s)	$0.000\times10^{+00}$	0.000	−47.000/
(R9)	$O(s) + CO(s) => CO_2(s) + Rh(s)$	$6.183\times10^{+21}$	0.034	129.982
	COV/CO(s)	$0.000\times10^{+00}$	0.000	−47.000/
(R10)	$CO_2(s) + Rh(s) => O(s) + CO(s)$	$5.752\times10^{+22}$	−0.175	106.492

85%. The reactor response to the feed stream temperature, velocity oscillation is in an efficient way that can tolerate 50% overload and drop load (50% increase and decrease in the mass flow rate). In such cases, the conversion for both methane and hydrogen still remains almost 80%.

The spatial temperature in the designed combustor is obtained below 1500 K. This temperature is considered low for the formation of NO and prompt NO [39–41]. The negligible contribution of gas phase reaction in the operation of the catalyst leaves no room for dissociation of nitrogen and attack of the hydrocarbon radicals to nitrogen.

Effect of catalyst

The influence of different catalysts including Platinum, Rhodium, Palladium and Palladium oxide- are considered to determine the operation of designed catalytic reactor in combustion of hydrogen, methane, and carbon monoxide for intalox pellets. The characteristics of the employed surface chemical reactions for the analysis of different catalyst are given Table 4. The chemistry set and list of chemical reactions are given in the appendix at the end of the manuscript.

The spanwise time-averaged rate of fuel consumption along the

Table F4
CO/O_2/Pt combustion mechanism, $k = AT^n\exp(-E/RT)$.

No	Reaction	A (cm, mol, s)	n	E (kJ mol^{-1})
(R1)	$O_2 + (Pt) => O_2(Pt)$	5.000×10^{-02}	0.000	0.000
(R2)	$O_2(Pt) => (Pt) + O_2$	$5.243\times10^{+11}$	−0.069	19.573
(R3)	$O_2(Pt) + (Pt) => O(Pt) + O(Pt)$	$8.325\times10^{+13}$	−0.000	39.933
(R4)	$O(Pt) + O(Pt) => O_2(Pt) + (Pt)$	$4.444\times10^{+21}$	0.000	264.067
	COV/O(Pt)	$0.000\times10^{+00}$	0.000	−88.200/
(R5)	$CO + (Pt) => CO(Pt)$	8.400×10^{-01}	0.000	0.000
(R6)	$CO(Pt) => (Pt) + CO$	$7.635\times10^{+12}$	−0.139	143.145
	COV/CO(Pt)	$0.000\times10^{+00}$	0.000	−29.300/
(R7)	$CO_2 + (Pt) => CO_2(Pt)$	3.193×10^{-03}	−0.035	2.686
(R8)	$CO_2(Pt) => (Pt) + CO_2$	$1.894\times10^{+10}$	0.139	21.855
(R9)	$CO(Pt) + O_2(Pt) => CO_2(Pt) + O(Pt)$	$4.124\times10^{+13}$	0.069	9.494
	COV/O(Pt)	$0.000\times10^{+00}$	0.000	44.100/
(R10)	$CO_2(Pt) + O(Pt) => CO(Pt) + O2(Pt)$	$2.910\times10^{+23}$	−0.069	272.506
	COV/CO(Pt)	$0.000\times10^{+00}$	0.000	29.300/
(R11)	$CO(Pt) + O(Pt) => CO_2(Pt) + (Pt)$	$4.764\times10^{+13}$	0.069	101.361
	COV/CO(Pt)	$0.000\times10^{+00}$	0.000	−29.300/
(R12)	$CO_2(Pt) + (Pt) => CO(Pt) + O(Pt)$	$6.297\times10^{+20}$	−0.069	140.239
	COV/O(Pt)	$0.000\times10^{+00}$	0.000	44.100/

Table F5
$CH_4/H_2/CO/O_2$/Ni combustion mechanism, $k = AT^n\exp(-E/RT)$.

No	Reaction	A (cm, mol, s)	N	E (kJ mol^{-1})
	$H_2 + 2NI(s) => 2H(s)$	1.000×10^{-002}	0.00	0.0
	$2H(s) => H_2 + 2NI(s)$	$2.545\times10^{+019}$	0.00	81.2
	$O_2 + 2NI(s) => 2O(s)$	1.000×10^{-002}	0.00	0.0
	$2O(s) => O_2 + 2NI(s)$	$4.283\times10^{+023}$	0.00	474.9
	$CH_4 + NI(s) => CH_4(s)$	8.000×10^{-003}	0.00	0.0
	$CH_4(s) => CH_4 + NI(s)$	$8.705\times10^{+015}$	0.00	37.5
	$H_2O + NI(s) => H_2O(s)$	1.000×10^{-001}	0.00	0.0
	$H_2O(s) => H_2O + NI(s)$	$3.732\times10^{+012}$	0.00	60.8
	$CO_2 + NI(s) => CO_2(s)$	1.000×10^{-005}	0.00	0.0
	$CO_2(s) => CO_2 + NI(s)$	$6.447\times10^{+007}$	0.00	26.0
	$CO + NI(s) => CO(s)$	5.000×10^{-001}	0.00	0.0
	$CO(s) => CO + NI(s)$	$3.563\times10^{+011}$	0.00	111.3
	COV/CO(s)	$0.000\times10^{+000}$	0.00	−50.0/
	$H(s) + O(s) => NI(s) + OH(s)$	$5.000\times10^{+022}$	0.00	97.9
	$NI(s) + OH(s) => H(s) + O(s)$	$1.781\times10^{+021}$	0.00	36.1
	$H(s) + OH(s) => NI(s) + H_2O(s)$	$3.000\times10^{+020}$	0.00	42.7
	$NI(s) + H_2O(s) => H(s) + H(s)$	$2.271\times10^{+021}$	0.00	91.8
	$2OH(s) => H_2O(s) + O(s)$	$3.000\times10^{+021}$	0.00	100.0
	$H_2O(s) + O(s) => 2OH(s)$	$6.373\times10^{+023}$	0.00	210.9
	$C(s) + O(s) => NI(s) + CO(s)$	$5.200\times10^{+023}$	0.00	148.1
	$NI(s) + CO(s) => C(s) + O(s)$	$1.354\times10^{+022}$	−3.00	116.1
	COV/CO(s)	$0.000\times10^{+000}$	0.00	−50.0/
	$CO(s) + O(s) => NI(s) + CO_2(s)$	$2.000\times10^{+019}$	0.00	123.6
	COV/CO(s)	$0.000\times10^{+000}$	0.00	−50.0/
	$NI(s) + CO_2(s) => CO(s) + O(s)$	$4.653\times10^{+023}$	−1.00	89.3
	$NI(s) + HCO(s) => H(s) + CO(s)$	$3.700\times10^{+021}$	0.00	0.0
	COV/CO(s)	$0.000\times10^{+000}$	0.00	50.0/
	$H(s) + CO(s) => NI(s) + HCO(s)$	$4.019\times10^{+020}$	−1.00	132.2
	$NI(s) + HCO(s) => CH(s) + O(s)$	$3.700\times10^{+024}$	−3.00	95.8
	$CH(s) + O(s) => NI(s) + HCO(s)$	$4.604\times10^{+020}$	0.00	110.0
	$NI(s) + CH_4(s) => H(s) + CH_3(s)$	$3.700\times10^{+021}$	0.00	57.7
	$H(s) + CH_3(s) => NI(s) + CH_4(s)$	$6.034\times10^{+021}$	0.00	61.6
	$NI(s) + CH_3(s) => H(s) + CH_2(s)$	$3.700\times10^{+024}$	0.00	100.0
	$H(s) + CH_2(s) => NI(s) + CH_3(s)$	$1.293\times10^{+023}$	0.00	55.3
	$NI(s) + CH_2(s) => H(s) + CH(s)$	$3.700\times10^{+024}$	0.00	97.1
	$H(s) + CH(s) => NI(s) + CH_2(s)$	$4.089\times10^{+024}$	0.00	79.2
	$NI(s) + CH(s) => H(s) + C(s)$	$3.700\times10^{+021}$	0.00	18.8
	$H(s) + C(s) => NI(s) + CH(s)$	$4.562\times10^{+022}$	0.00	161.1
	$CH_4(s) + O(s) => OH(s) + CH_3(s)$	$1.700\times10^{+024}$	0.00	88.3
	$OH(s) + CH_3(s) => CH_4(s) + O(s)$	$9.876\times10^{+022}$	0.00	30.4
	$CH_3(s) + O(s) => OH(s) + CH_2(s)$	$3.700\times10^{+024}$	0.00	130.1
	$OH(s) + CH_2(s) => CH_3(s) + O(s)$	$4.607\times10^{+021}$	0.00	23.6
	$CH_2(s) + O(s) => OH(s) + CH(s)$	$3.700\times10^{+024}$	0.00	126.8
	$OH(s) + CH(s) => CH_2(s) + O(s)$	$1.457\times10^{+023}$	0.00	47.1
	$CH(s) + O(s) => OH(s) + C(s)$	$3.700\times10^{+021}$	0.00	48.1
	$OH(s) + C(s) => CH(s) + O(s)$	$1.625\times10^{+021}$	0.00	128.6

reactor is given in Fig. 7 for different combustion systems-H_2 rhodium, H_2 palladium and CO rhodium. The designed reactor can burn hydrogen and carbon monoxide on the surface of precious metals such as rhodium and palladium. The findings, not shown here, confirmed that the combustion efficiency of these systems is up to 90% at the combustor outlet plane. As the trendlines in Fig. 7 exhibits, the converter most reactive zone is from 0 to 20 mm where the surface reactions are at the maximum rate of occurrence. The combustion in all of the cases is taking place at near 1300 K with surface catalytic reaction prevailing the gas phase reaction. The gas phase reactions, if any are volumetric as the temperature within the convertor does not go beyond the ignition flame temperature of the fuels.

Transient analysis of the bed

How well the designed microcombustor will behave in time can be addressed by transient analysis of the bed in progressing the combustion and to burn the fuels. The premix mixture of methane, hydrogen and oxygen will be injected to the reactor where they will be adsorbed to the

Table F6
$CH_4/H_2/CO/O_2$/Pd combustion mechanism, $k = AT^n\exp(-E/RT)$.

No	Reaction	A (cm, mol, s)	n	E (kcal mol^{-1})
(R1)	$H_2 + Pd(s) + Pd(s) => H(s) + H(s)$	2.445×10^{-01}	−0.076	0.000
(R2)	$O_2 + Pd(s) + Pd(s) => O(s) + O(s)$	5.712×10^{-02}	0.012	1.945
(R3)	$CH_4 + Pd(s) => CH_4(s)$	8.557×10^{-03}	0.017	0.000
(R4)	$H_2O + Pd(s) => H_2O(s)$	1.402×10^{-01}	0.033	0.000
(R5)	$CO_2 + Pd(s) => CO_2(s)$	8.186×10^{-03}	−0.037	0.000
(R6)	$CO + Pd(s) => CO(s)$	6.716×10^{-01}	0.015	0.935
(R7)	$CH_4 + O(s) + O(s) => H_3CO(s) + OH(s)$	8.928×10^{-03}	0.004	159.978
	COV/O(s)	$0.000\times10^{+00}$	0.000	−22.500/
(R8)	$H(s) + H(s) => Pd(s) + Pd(s) + H_2$	$8.393\times10^{+19}$	0.303	85.036
(R9)	$O(s) + O(s) => Pd(s) + Pd(s) + O_2$	$2.932\times10^{+22}$	−0.049	221.818
	COV/O(s)	$0.000\times10^{+00}$	0.000	−22.500/
(R10)	$H_2O(s) => Pd(s) + H_2O$	$1.244\times10^{+14}$	−0.134	46.593
(R11)	$CO(s) => Pd(s) + CO$	$8.565\times10^{+13}$	−0.062	138.558
	COV/CO(s)	$0.000\times10^{+00}$	0.000	−31.000/
(R12)	$CO_2(s) => Pd(s) + CO_2$	$1.392\times10^{+12}$	0.146	23.156
(R13)	$CH_4(s) => Pd(s) + CH_4$	$1.865\times10^{+13}$	−0.068	29.499
(R14)	$H_3CO(s) + OH(s) => O(s) + O(s) + CH_4$	$2.046\times10^{+18}$	−0.017	248.686
(R15)	$O(s) + H(s) => OH(s) + Pd(s)$	$3.598\times10^{+22}$	−0.060	85.044
	COV/O(s)	$0.000\times10^{+00}$	0.000	−11.250/
(R16)	$OH(s) + Pd(s) => O(s) + H(s)$	$4.169\times10^{+20}$	0.060	66.456
(R17)	$OH(s) + H(s) => H_2O(s) + Pd(s)$	$3.017\times10^{+20}$	−0.059	−0.823
(R18)	$H_2O(s) + Pd(s) => OH(s) + H(s)$	$4.972\times10^{+22}$	0.059	109.623
(R19)	$OH(s) + OH(s) => O(s) + H_2O(s)$	$2.516\times10^{+19}$	0.001	54.533
(R20)	$O(s) + H_2O(s) => OH(s) + OH(s)$	$3.578\times10^{+23}$	−0.001	183.567
	COV/O(s)	$0.000\times10^{+00}$	0.000	−11.250/
(R21)	$O(s) + C(s) => CO(s) + Pd(s)$	$5.434\times10^{+23}$	0.004	21.097
	COV/O(s)	$0.000\times10^{+00}$	0.000	−11.250/
(R22)	$CO(s) + Pd(s) => O(s) + C(s)$	$2.392\times10^{+21}$	−0.004	214.903
	COV/CO(s)	$0.000\times10^{+00}$	0.000	−31.000/
(R23)	$O(s) + CO(s) => CO_2(s) + Pd(s)$	$6.874\times10^{+18}$	0.052	71.247
	COV/O(s)	$0.000\times10^{+00}$	0.000	−11.250/
	COV/CO(s)	$0.000\times10^{+00}$	0.000	−31.000/
(R24)	$CO_2(s) + Pd(s) => O(s) + CO(s)$	$2.400\times10^{+21}$	−0.052	132.753
(R25)	$CH_4(s) + Pd(s) => CH_3(s) + H(s)$	$1.301\times10^{+22}$	0.064	66.978
(R26)	$CH_3(s) + H(s) => CH_4(s) + Pd(s)$	$1.052\times10^{+21}$	−0.064	38.422
(R27)	$CH_3(s) + Pd(s) => CH_2(s) + H(s)$	$2.811\times10^{+24}$	0.064	104.253
(R28)	$CH_2(s) + H(s) => CH_3(s) + Pd(s)$	$4.871\times10^{+21}$	−0.064	37.147
(R29)	$CH_2(s) + Pd(s) => CH(s) + H(s)$	$8.888\times10^{+23}$	0.064	100.278
(R30)	$CH(s) + H(s) => CH_2(s) + Pd(s)$	$1.540\times10^{+25}$	−0.064	63.722
(R31)	$CH(s) + Pd(s) => C(s) + H(s)$	$2.811\times10^{+23}$	0.064	20.753
(R32)	$C(s) + H(s) => CH(s) + Pd(s)$	$4.871\times10^{+24}$	−0.064	165.847
(R33)	$O(s) + CH_4(s) => CH_3(s) + OH(s)$	$2.591\times10^{+24}$	0.004	96.622
	COV/O(s)	$0.000\times10^{+00}$	0.000	−11.250/
(R34)	$CH_3(s) + OH(s) => O(s) + CH_4(s)$	$2.427\times10^{+21}$	−0.004	49.478
(R35)	$O(s) + CH_3(s) => CH_2(s) + OH(s)$	$2.611\times10^{+25}$	0.004	97.347
	COV/O(s)	$0.000\times10^{+00}$	0.000	−11.250/
(R36)	$CH_2(s) + OH(s) => O(s) + CH_3(s)$	$5.243\times10^{+20}$	−0.004	11.653
(R37)	$O(s) + CH_2(s) => CH(s) + OH(s)$	$8.257\times10^{+21}$	0.004	88.322

(*continued on next page*)

Table F6 (*continued*)

No	Reaction	A (cm, mol, s)	n	E (kcal mol^{-1})
	COV/O(s)	0.000×10^{+00}	0.000	−11.250/
(R38)	CH(s) + OH(s) => O(s) + CH_2(s)	1.658×10^{+21}	−0.004	33.178
(R39)	O(s) + CH(s) => C(s) + OH (s)	2.611×10^{+21}	0.004	36.847
	COV/O(s)	0.000×10^{+00}	0.000	−11.250/
(R40)	C(s) + OH(s) => O(s) + CH (s)	5.243×10^{+20}	−0.004	163.353
(R41)	C(s) + OH(s) => CO(s) + H (s)	1.898×10^{+22}	0.064	0.503
(R42)	CO(s) + H(s) => C(s) + OH (s)	7.213×10^{+21}	−0.064	212.897
	COV/CO(s)	0.000×10^{+00}	0.000	−31.000/
(R43)	H_3CO(s) + O(s) => H_2CO(s) + OH(s)	2.351×10^{+24}	0.017	65.714
	COV/O(s)	0.000×10^{+00}	0.000	−11.250/
(R44)	H_2CO(s) + OH(s) => H_3CO (s) + O(s)	5.824×10^{+21}	−0.017	56.886
(R45)	H2CO(s) + O(s) => HCO(s) + OH(s)	2.351×10^{+24}	0.017	31.014
	COV/O(s)	0.000×10^{+00}	0.000	−11.250/
(R46)	HCO(s) + OH(s) => H_2CO (s) + O(s)	5.824×10^{+21}	−0.017	14.986
(R47)	HCO(s) + O(s) => CO(s) + OH(s)	2.351×10^{+24}	0.017	12.114
	COV/O(s)	0.000×10^{+00}	0.000	−11.250/
(R48)	CO(s) + OH(s) => HCO(s) + O(s)	5.824×10^{+21}	−0.017	111.186
	COV/CO(s)	0.000×10^{+00}	0.000	−31.000/
(R49)	CO(s) + OH(s) => COOH(s) + Pd(s)	4.167×10^{+19}	0.018	46.493
	COV/CO(s)	0.000×10^{+00}	0.000	−31.000/
(R50)	COOH(s) + Pd(s) => CO(s) + OH(s)	3.251×10^{+21}	−0.018	27.807
(R51)	COOH(s) + Pd(s) => CO_2(s) + H(s)	1.871×10^{+19}	0.094	27.009
(R52)	CO_2(s) + H(s) => COOH(s) + Pd(s)	7.228×10^{+21}	−0.094	125.791
(R53)	COOH(s) + H(s) => CO(s) + H_2O(s)	2.532×10^{+18}	−0.076	61.084
(R54)	CO(s) + H_2O(s) => COOH (s) + H(s)	5.349×10^{+18}	0.076	190.216
	COV/CO(s)	0.000×10^{+00}	0.000	−31.000/

surface of catalyst for the combustion with concomitant desorption of water vapor and carbon dioxide which will exit from hot end of the reactor. The Damköhler number (Da) is used here to show the capability of the reactor to simultaneously burn the hydrogen and methane. It is the ratio of the turbulent timescale to the chemical reaction timescale. It has been estimated for methane, hydrogen and OH as the following.

$$Da \sim \frac{\text{mixing time scale}}{\text{chemical time scale}} \tag{13}$$

The mixing rate is estimated from the turbulent mixing of the components in the gas phase and surface chemical reactions associated with the those considered species in the turbulent mixing are for the chemical time scales. The hydrogen is destructed through the surface reaction R1 ($H_2 + 2PT(S) \Rightarrow 2H(S)$) and a possibility for surface formation and desorption exists from R2 ($2H(S) \Rightarrow H_2 + 2PT(S)$). The OH will be produced and consumed R8 ($OH + PT(S) \Rightarrow OH(S)$) and R9 ($OH(S) \Rightarrow OH + PT(S)$), respectively. The methane is also consumed only from the reaction R17 ($CH_4 + 2PT(S) \Rightarrow CH_3(S) + H(S)$). In laminar flow through the catalytic converter, Da can be estimated from the ratio of advection to reaction source terms for the species. The results of the Da analysis at different times when the feedstock is injected to the reactor are presented in Fig. 8.

The Da number is averaged for fuel species and hydroxyl at 20 transverse planes along the reactor starting from the part of reactor loaded with catalysts. The distance between the planes was 20 mm. In

Table F7
$CH_4/H_2/CO/O_2$/PdO combustion mechanism, $k = AT^n \exp(-E/RT)$.

No	Reaction	A (cm, mol, s)	n	E (kcal mol^{-1})
(R1)	CH_4 + PdO + PdO => CH_3(s) + H(s)	4.582E-02	−0.001	33.155
(R2)	CH_3(a) + H(b) => PdO + PdO + CH_4	1.034E + 21	0.003	106.180
(R3)	CH_4 + (s) + OH(s) => CH_3(s) + H_2O(s)	1.510E-02	0.001	28.860
(R4)	CH_3(s) + H_2O(s) => OH(s) + PdO + CH_4	7.071E + 19	−0.004	104.259
(R5)	CH_4 + PdO + O(s) => CH_3(s) + OH(s)	3.082E-02	0.007	26.234
(R6)	CH_3(s) + OH(s) => O(s) + PdO + CH_4	2.695E + 20	−0.029	192.865
(R7)	O_2 + PdO => O_2(s)	5.710E-02	0.000	0.000
(R8)	O_2(a) => (a) + O_2	6.702E + 15	−0.031	63.541
(R9)	O_2 + PdO => O(b)	5.710E-02	0.000	0.000
(R10)	O(b) => PdO + O_2	7.024E + 15	−0.027	159.975
(R11)	H_2O + PdO + O(s) => OH(s) + OH(s)	1.400E-01	0.000	0.000
(R12)	OH(s) + OH(s) => O(s) + PdO + H_2O	3.307E + 21	0.013	191.178
(R13)	H_2O + PdO => H_2O(s)	1.400E-01	0.000	0.000
(R14)	H_2O(s) => PdO + H_2O	6.293E + 12	0.045	99.946
(R15)	CO_2 + PdO => CO_2(s)	4.910E-02	0.000	0.000
(R16)	CO_2(s) => PdO + CO_2	4.087E + 14	0.029	65.097
(R17)	CH_3(s) + PdO => PdO + CH_3(s)	1.494E + 22	0.008	131.139
(R18)	PdO + CH_3(s) => CH_3(s) + PdO	2.441E + 23	−0.008	181.201
(R19)	O(s) + CH_3(s) => OH(s) + CH_2(s)	1.250E + 22	0.012	33.366
(R20)	OH(s) + CH_2(s) => O(s) + CH_3(s)	1.855E + 22	−0.012	303.074
(R21)	OH(s) + CH_3(s) => H_2O(s) + CH_2(s)	1.398E + 22	−0.004	33.193
(R22)	H_2O(s) + CH_2(s) => OH(s) + CH_3(s)	1.111E + 22	0.004	211.667
(R23)	CH_3(s) + O(s) => CH_2OH(s) + PdO	3.534E + 21	0.016	30.953
(R24)	CH_2OH(s) + PdO => CH_3(s) + O(s)	2.466E + 23	−0.016	333.447
(R25)	CH_3(s) + OH(s) => CH_2(s) + H_2O(s)	2.014E + 21	0.004	73.229
(R26)	CH_2(s) + H_2O(s) => CH_3(s) + OH(s)	1.175E + 22	−0.004	116.851
(R27)	CH_2(s) + OH(s) => CH_2OH(s) + PdO	3.420E + 21	−0.004	12.581
(R28)	CH_2OH(s) + PdO => CH_2(s) + OH(s)	2.191E + 22	0.004	180.219
(R29)	CH_2OH(a) + PdO => CH_2O(s) + H(s)	1.917E + 22	0.012	12.654
(R30)	CH_2O(s) + H(s) => CH_2OH(s) + PdO	3.348E + 20	−0.012	57.646
(R31)	CH_2O(s) + OH(s) => CHO(s) + H_2O(s)	5.608E + 21	0.012	51.570
(R32)	CHO(s) + H_2O(s) => CH_2O(s) + OH(s)	2.119E + 22	−0.012	192.230
(R33)	CHO(s) + OH(s) => CO(s) + H_2O(s)	5.921E + 22	0.008	65.968
(R34)	CO(s) + H2O(s) => CHO(s) + OH(s)	8.990E + 21	−0.008	267.532
(R35)	CH_3(s) + PdO => CH_2(s) + H (s)	1.827E + 21	0.000	123.976
(R36)	CH_2(s) + H(s) => CH_3(s) + PdO	5.137E + 22	−0.000	165.224
(R37)	CH_2(s) + PdO => PdO + CH2 (s)	1.257E + 22	0.000	13.103
(R38)	PdO + CH_2(s) => CH_2(s) + PdO	2.797E + 22	−0.000	198.017

(*continued on next page*)

Table F7 (*continued*)

No	Reaction	A (cm, mol, s)	n	E (kcal mol^{-1})
(R39)	$CH_2(s) + PdO => CH(s) + H(s)$	3.793E + 22	0.008	112.541
(R40)	$CH(a) + H(s) => CH_2(s) + PdO$	2.987E + 22	−0.008	163.159
(R41)	$CH(s) + PdO => CHO(s) + PdO$	2.103E + 21	0.008	24.821
(R42)	$CHO(s) + PdO => CH(s) + PdO$	1.218E + 21	−0.008	215.219
(R43)	$PdO + CH_2(s) => CH_2O(s) + PdO$	2.155E + 22	0.008	91.222
(R44)	$CH_2O(s) + PdO => PdO + CH_2(s)$	2.425E + 20	−0.008	9.038
(R45)	$CH_2O(s) + PdO => CHO(s) + H(s)$	3.274E + 21	0.008	69.676
(R46)	$CHO(s) + H(s) => CH_2O(s) + PdO$	5.962E + 22	−0.008	207.964
(R47)	$CHO(s) + PdO => CO(s) + H(s)$	1.088E + 23	0.004	55.610
(R48)	$CO(s) + H(s) => CHO(s) + PdO$	7.956E + 22	−0.004	254.800
(R49)	$CHO(s) + PdO => PdO + CHO(s)$	2.746E + 22	0.018	76.549
(R50)	$PdO + CHO(s) => CHO(s) + PdO$	6.754E + 21	−0.018	106.611
(R51)	$PdO + CHO(s) => H(s) + CO(s)$	2.732E + 21	−0.002	141.937
(R52)	$H(s) + CO(s) => PdO + CHO(s)$	2.123E + 21	0.002	263.113
(R53)	$CO(s) + PdO => PdO + CO(s)$	1.313E + 21	0.011	33.868
(R54)	$PdO + CO(s) => CO(s) + PdO$	2.212E + 21	−0.011	16.262
(R55)	$PdO + CO(s) => CO_2(s) + PdO$	1.410E + 21	0.010	42.023
(R56)	$CO_2(s) + PdO => PdO + CO(s)$	9.554E + 20	−0.010	78.477
(R57)	$PdO + H(s) => OH(s) + PdO$	1.886E + 22	0.000	137.800
(R58)	$OH(s) + PdO => PdO + H(s)$	4.222E + 21	0.000	27.900
(R59)	$O_2(s) + PdO => O(s) + O(s)$	3.815E + 22	0.005	174.961
(R60)	$O(s) + O(s) => O_2(s) + PdO$	1.744E + 21	−0.005	59.139
(R61)	$PdO + O(s) => O(s) + PdO$	2.380E + 22	0.027	116.625
(R62)	$O(s) + PdO => PdO + O(s)$	1.797E + 21	−0.027	107.875
(R63)	$O(s) + PdO => PdO + PdO$	8.012E + 21	0.020	48.597
(R64)	$PdO + PdO => O(s) + PdO$	1.387E + 22	−0.020	252.103
(R65)	$O_2(s) + PdO => O(s) + PdO$	1.196E + 24	0.025	81.408
(R66)	$O(s) + PdO => O_2(s) + PdO$	9.469E + 22	−0.025	169.092
(R67)	$PdO + H(s) => H(s) + PdO$	6.133E + 22	0.002	148.173
(R68)	$H(s) + PdO => PdO + H(s)$	9.505E + 21	−0.002	117.827
(R69)	$OH(s) + CHO(s) => H_2O(s) + CO(s)$	2.992E + 22	0.001	2.168
(R70)	$H_2O(s) + CO(s) => OH(s) + CHO(s)$	3.113E + 22	−0.001	156.062
(R71)	$PdO + CHO(s) => HCOO(s) + PdO$	3.658E + 21	0.000	11.580
(R72)	$HCOO(s) + PdO => PdO + CHO(s)$	1.210E + 21	0.000	8.680
(R73)	$HCOO(s) + OH(s) => CO_2(s) + H_2O(s)$	2.305E + 23	0.011	183.191
(R74)	$CO_2(s) + H2O(s) => HCOO(s) + OH(s)$	4.912E + 23	−0.011	376.439
(R75)	$HCOO(s) + PdO => CO_2(s) + H(s)$	1.681E + 23	0.007	177.623
(R76)	$CO_2(s) + H(s) => HCOO(s) + PdO$	1.726E + 24	−0.007	368.497
(R77)	$H_2O(s) + PdO <=> OH(s) + H(s)$	3.659E + 21	0.000	12.500

fuel species (H_2 vs CH_4) Da for hydrogen is slightly more than the methane which is likely due to more propensity of reactor catalyst to absorb and combust hydrogen. Da for methane is almost constant along the reactor while it shows an increasing trend towards hot end. For flame marker OH, similar to fuel species, Da also remains within a limited bound and does not go beyond 10. Indeed, the affinity of the surface catalyst for OH is higher to remove the main flame marker from the gas phase, possibly resulting in more intense surface than gaseous phase reactions. The spatial Da also demonstrates that the evolution of the combustion is from the surface of catalysts locating everywhere in the chamber. The length is sufficient to achieve around 90% combustion efficiency and 93% effectiveness factor in the case of intalox saddle. The Da for other case studies (catalyst pellets and monolith), not shown here, demonstrates that the designed reaction is with appropriate dimensions to maintain overall combustion over the entire length of the combustor at temperature near the ignition temperatures. At such a temperature, the gaseous reaction phase, if any, evolves throughout the entire combustor volume and combustion is nearly flameless. The reactor temperature was below stoichiometric mixture temperature.

Conclusions

This work delivers a new proof of concept for the invention of catalytic microcombustors to burn syngas. The DNS and finite chemistry were applied to model the reactive flow within the designed combustor and to analyse the combustion performance under different operating conditions. Under the first phase of the design procedure, the premix combustion within the micocombustor is evaluated to maintain low NO_X emission, the combustor ability to light, toleration of sudden changes in power loads, efficient combustion, and achievement of the required life span by using various design parameters. Within twelve different shapes of catalyst pellet and four monolithic structures, the microcombustor demonstrates the best combustion performance with the catalyst in the shape of intalox saddle with a combined least possible pressure drop and maximum combustion efficiency. The designed reactor is also well able to respond to the variation in fuel composition and catalyst material, temperature and mass flow rate fluctuations by maintaining the combustion efficiency of more than 90%. The microcombustor can control the combustion on the surface of the catalyst and limit the gaseous phase reactions with proper equivalence ratio.

The evolution of surface averaged Da demonstrates that the entire 200 mm reactor is well able to participate in the dissociation reaction without leaving any part ineffective and appearance of both cold and hot spots. The low spatial gaseous concentrations of OH gives rise to comparatively higher contribution of the surface reactions in the combustion. Here, the combustion is uniform and no significant rise in combustion temperature in the gas phase is observed throughout the reactor.

The fluid structure inside of the packed bed reactors is very complex, especially when as fluid channeling, fluid-solid interactions are intermingled with the stochastic nature of the fluid motion. To provide a thorough and comprehensive analysis, the reactor should be built and experimented using proper laser diagnostic techniques, the models should be validated, and employed to delve into the physics and thermochemical state of the combustion within the designed micro combustor.

Declaration of Competing Interest

The authors declare that they have no known competing financial interests or personal relationships that could have appeared to influence the work reported in this paper.

Data availability

Data will be made available on request.

Acknowledgements

Data for this aricle can be accessed through the Brunel University London repository at: https://doi.org/10.17633/rd.brunel.23706051.v1.

Appendix A. Random pack illustration[3]

Random Pack 1
Fig. A1.
Random Pack 2
Fig. A2.
Random Pack 3
Fig. A3.

Appendix B. Structured bed illustration

Structured Pack 1
Fig. B1.
Structured Pack 2
Fig. B2.

Appendix C. Packing illustration

Fig. C1
Appendix D Monolith illustration
Fig. D1.
Appendix E Surface chemistry
Fig. E1.

Appendix F. Surface chemistry

Hydrogen (H_2) surface dissociation chemistry set on Pd/Rh.
Tables F1 and F2.
Carbon monoxide (CO) surface dissociation chemistry set on Pd/Rh.
Tables F3 and F4.
Syngas ($CH_4/H_2/CO$) surface dissociation chemistry set on Pd/Rh.
Tables F5 – F7.

References

[1] Bazooyar B, Ghorbani A, Shariati A. Physical properties of methyl esters made from alkali-based transesterification and conventional diesel fuel, Energy Sources. Part A Recover Util Environ Eff 2015;37:468–76. https://doi.org/10.1080/15567036.2011.586975.
[2] Miesse CM, Masel RI, Jensen CD, Shannon MA, Short M. Submillimeter-scale combustion. AIChE J 2004;50:3206–14. https://doi.org/10.1002/aic.10271.
[3] Yedala N, Raghu AK, Kaisare NS. A 3D CFD study of homogeneous-catalytic combustion of hydrogen in a spiral microreactor. Combust Flame 2019;206:441–50. https://doi.org/10.1016/j.combustflame.2019.05.022.
[4] Kaisare NS, Deshmukh SR, Vlachos DG. Stability and performance of catalytic microreactors: Simulations of propane catalytic combustion on Pt. Chem Eng Sci 2008;63:1098–116. https://doi.org/10.1016/j.ces.2007.11.014.
[5] Regatte VR, Selle G, Kaisare NS. The role of homogeneous chemistry during Ignition of propane combustion in Pt-catalyzed microburners. Int J Spray Combust Dyn 2012;4:155–74. https://doi.org/10.1260/1756-8277.4.2.155.
[6] Pizza G, Mantzaras J, Frouzakis CE, Tomboulides AG, Boulouchos K. Suppression of combustion instabilities of premixed hydrogen/air flames in microchannels using heterogeneous reactions. Proc Combust Inst 2009;32 I I:3051–8. https://doi.org/10.1016/j.proci.2008.05.055.
[7] Lloyd SA, Weinberg FJ. A burner for mixtures of very low heat content. Nature 1974;251:47–9. https://doi.org/10.1038/251047a0.
[8] Aghalayam P, Vlachos DG. Roles of thermal and radical quenching in emissions of wall-stabilized hydrogen flames. AIChE J 1998;44:2025–34. https://doi.org/10.1002/aic.690440910.
[9] Deshmukh SR, Vlachos DG. Effect of flow configuration on the operation of coupled combustor/reformer microdevices for hydrogen production. Chem Eng Sci 2005;60:5718–28. https://doi.org/10.1016/j.ces.2005.04.082.
[10] Federici JA, Norton DG, Brüggemann T, Voit KW, Wetzel ED, Vlachos DG. Catalytic microcombustors with integrated thermoelectric elements for portable power production. J Power Sources 2006;161:1469–78. https://doi.org/10.1016/j.jpowsour.2006.06.042.
[11] Bazooyar B, Gohari Darabkhani H. Analysis of flame stabilization to a thermo-photovoltaic micro-combustor step in turbulent premixed hydrogen flame. Fuel 2019;257:115989.
[12] Ganley JC, Seebauer EG, Masel RI. Porous Anodic Alumina Microreactors for Production of Hydrogen from Ammonia. AIChE J 2004;50:829–34. https://doi.org/10.1002/aic.10078.
[13] Ghorbani A, Bazooyar B. Optimization of the combustion of SOME (soybean oil methyl ester), B5, B10, B20 and petrodiesel in a semi industrial boiler. Energy 2012;44:217–27. https://doi.org/10.1016/j.energy.2012.06.035.
[14] Bazooyar B, Gohari Darabkhani H. The design strategy and testing of an efficient microgas turbine combustor for biogas fuel. Fuel 2021;294:120535. https://doi.org/10.1016/j.fuel.2021.120535.
[15] Bazooyar B, Shariati A, Khosravi-Nikou M, Hashemabadi SH. Numerical analysis of nitrogen oxides in turbulent lifted H2/N2 cabra jet flame issuing into a vitiated coflow. Int J Hydrogen Energy 2019;44:13932–52. https://doi.org/10.1016/j.ijhydene.2019.03.166.
[16] Bazooyar B, Darabkhani HG. Design and numerical analysis of a 3 kWe flameless microturbine combustor for hydrogen fuel. Int J Hydrogen Energy 2019;44:11134–44. https://doi.org/10.1016/j.ijhydene.2019.02.132.
[17] Maruta K, Takeda K, Ahn J, Borer K, Sitzki L, Ronney PD, et al. Extinction limits of catalytic combustion in microchannels. Proc Combust Inst 2002;29:957–63. https://doi.org/10.1016/S1540-7489(02)80121-3.
[18] Bazooyar B, Jomekian A, Karimi-Sibaki E, Habibi M, Gohari Darabkhani H. The role of heat recirculation and flame stabilization in the formation of NOX in a thermo-photovoltaic micro-combustor step wall. Int J Hydrogen Energy 2019;44:26012–27. https://doi.org/10.1016/j.ijhydene.2019.08.061.
[19] Lloyd SA, Weinberg FJ. Limits to energy release and utilisation from chemical fuels. Nature 1975;257:367–70. https://doi.org/10.1038/257367a0.
[20] Raimondeau S, Norton D, Vlachos DG, Masel RI. Modeling of high-temperature microburners. Proc Combust Inst 2002;29:901–7. https://doi.org/10.1016/S1540-7489(02)80114-6.
[21] Ronney PD. Analysis of non-adiabatic heat-recirculating combustors. Combust Flame 2003;135:421–39. https://doi.org/10.1016/j.combustflame.2003.07.003.
[22] Darabkhani HG, Varasteh H, Bazooyar B. Carbon Capture Technologies for Gas-Turbine-Based Power Plants. Elsevier 2023. https://doi.org/10.1016/c2018-0-04100-6.
[23] Gonçalves A, Puna JF, Guerra L, Rodrigues JC, Gomes JF, Santos MT, et al. Towards the development of syngas/biomethane electrolytic production, using liquefied biomass and heterogeneous catalyst. Energies 2019;12. https://doi.org/10.3390/en12193787.
[24] Leach TT, Cadou CP. The role of structural heat exchange and heat loss in the design of efficient silicon micro-combustors. Proc Combust Inst 2005;30 I I:2437–44. https://doi.org/10.1016/j.proci.2004.08.229.
[25] Fernandez-Pello AC. Micropower generation using combustion: Issues and approaches. Proc Combust Inst 2002;29:883–99. https://doi.org/10.1016/s1540-7489(02)80113-4.
[26] Deutschmann O, Maier LI, Riedel U, Stroemman AH, Dibble RW. Hydrogen assisted catalytic combustion of methane on platinum. Catal Today 2000;59:141–50. https://doi.org/10.1016/S0920-5861(00)00279-0.
[27] Tomboulides AG, Lee JCY, Orszag SA. Numerical Simulation of Low Mach Number Reactive Flows. J Sci Comput 1997;12:139–67. https://doi.org/10.1023/A:1025669715376.
[28] Deville, MO, Fischer, PF, Mund , EH, Gartling, DK. High-Order Methods for Incompressible Fluid Flow. Appl Mech Rev 2003;56(3):B43–.
[29] Byrne GD, Hindmarsh AC. PVODE, an ODE solver for parallel computers. Int J High Perform Comput Appl 1999;13:354–65. https://doi.org/10.1177/109434209901300405.
[30] Bazooyar B, Hallajbashi N, Shariati A, Ghorbani A. An investigation of the effect of input air upon combustion performance and emissions of biodiesel and diesel fuel in an experimental boiler, Energy Sources. Part A Recover Util Environ Eff 2014;36:383–92. https://doi.org/10.1080/15567036.2010.538810.
[31] Bazooyar B, Shariati A. A comparison of the emission and thermal capacity of methyl ester of corn oil with diesel in an experimental boiler, Energy Sources. Part A Recover Util Environ Eff 2013;35:1618–28. https://doi.org/10.1080/15567036.2010.527902.
[32] Ghorbani A, Bazooyar B, Shariati A, Jokar SM, Ajami H, Naderi A. A comparative study of combustion performance and emission of biodiesel blends and diesel in an

[3] For random structure, the discrete element method (DEM) method was employed to analyse the behavior of packing upon filling the reactor using a Newton's law of motion and to provide a more realistic randomness in packing the combustor.

experimental boiler. Appl Energy 2011;88:4725–32. https://doi.org/10.1016/j.apenergy.2011.06.016.
[33] Bazooyar B, Ghorbani A, Shariati A. Combustion performance and emissions of petrodiesel and biodiesels based on various vegetable oils in a semi industrial boiler. Fuel 2011;90:3078–92. https://doi.org/10.1016/j.fuel.2011.05.025.
[34] Bazooyar B, Darabkhani HG. Design procedure and performance analysis of a microturbine combustor working on biogas for power generation. Proc ASME Turbo Expo 2019;4B–2019. https://doi.org/10.1115/GT2019-91052.
[35] Bazooyar B, Gohari Darabkhani H. Design, manufacture and test of a micro-turbine renewable energy combustor, Energy Convers. Manag 2020;213:112782. https://doi.org/10.1016/j.enconman.2020.112782.
[36] Bazooyar B, Gohari Darabkhani H. The design strategy and testing of an efficient microgas turbine combustor for biogas fuel. Fuel 2021;294:120535.
[37] Bazooyar B, Shariati A, Hashemabadi SH. Turbulent Non-premixed Combustion of Rapeseed Methyl Ester in a Free Shear Swirl Air Flow. Ind Eng Chem Res 2016;55:11645–63. https://doi.org/10.1021/acs.iecr.6b02500.
[38] Bazooyar B, Jomekian A, Shariati A. Analysis of the Formation and Interaction of Nitrogen Oxides in a Rapeseed Methyl Ester Nonpremixed Turbulent Flame. Energy Fuel 2017;31:8708–21. https://doi.org/10.1021/acs.energyfuels.7b01278.
[39] Bazooyar B, Ebrahimzadeh E, Jomekian A, Shariati A. NOx formation of biodiesel in utility power plant boilers. part a: Influence of fuel characteristics. Energy Fuel 2014;28:3778–92. https://doi.org/10.1021/ef500001g.
[40] Bazooyar B, Hashemabadi SH, Shariati A. NOX formation of biodiesel in utility power plant boilers; Part B. Comparison of NO between biodiesel and petrodiesel, Fuel 2016;182:323–32. https://doi.org/10.1016/j.fuel.2016.05.018.
[41] Bazooyar B, Shariati A, Hashemabadi SH. Characterization and Reduction of NO during the Combustion of Biodiesel in a Semi-industrial Boiler. Energy Fuel 2015;29:6804–14. https://doi.org/10.1021/acs.energyfuels.5b01529.
[42] Karakaya C, Deutschmann O. Kinetics of hydrogen oxidation on Rh/Al2O3 catalysts studied in a stagnation-flow reactor. Chem Eng Sci 2013;89:171–84. https://doi.org/10.1016/j.ces.2012.11.004.
[43] Deutschmann O, Schmidt R, Behrendt F, Warnat J. Numerical modeling of catalytic ignition. Symp Combust 1996;26:1747–54. https://doi.org/10.1016/S0082-0784(96)80400-0.
[44] Karadeniz H, Karakaya C, Tischer S, Deutschmann O. Numerical modeling of stagnation-flows on porous catalytic surfaces: CO oxidation on Rh/Al2O3. Chem Eng Sci 2013;104:899–907. https://doi.org/10.1016/j.ces.2013.09.038.
[45] Stotz H, Maier L, Deutschmann O. Methane Oxidation over Palladium: On the Mechanism in Fuel-Rich Mixtures at High Temperatures. Top Catal 2017;60:83–109. https://doi.org/10.1007/s11244-016-0717-5.
[46] Stotz H, Maier L, Boubnov A, Gremminger AT, Grunwaldt JD, Deutschmann O. Surface reaction kinetics of methane oxidation over PdO. J Catal 2019;370:152–75. https://doi.org/10.1016/j.jcat.2018.12.007.